The Meteoritical Society

Meteoritics & Planetary Science 1–24 (2015)
doi: 10.1111/maps.12463

The formation of IIE iron meteorites investigated by the chondrule-bearing Mont Dieu meteorite

N. VAN ROOSBROEK[1*], V. DEBAILLE[1], L. PITTARELLO[2], S. GODERIS[2,3], M. HUMAYUN[4], L. HECHT[5], F. JOURDAN[6], M. J. SPICUZZA[7], F. VANHAECKE[3], and Ph. CLAEYS[2]

[1]Laboratoire G-Time, Université Libre de Bruxelles, CP 160/02, 50 Avenue F. D. Roosevelt, Brussels B-1050, Belgium
[2]Earth System Science, Vrije Universiteit Brussel, Pleinlaan 2, Brussels B-1050, Belgium
[3]Department of Analytical Chemistry, Ghent University, Krijgslaan 281-S12, Ghent B-9000, Belgium
[4]Department of Earth, Ocean & Atmospheric Science and National High Magnetic Field Laboratory, Florida State University, Tallahassee, Florida 32310, USA
[5]Museum für Naturkunde, Leibniz-Institut für Evolutions-und Biodiversitätsforschung, Invalidenstraße 43, Berlin 10115, Germany
[6]Department of Applied Geology & JdL CMS, Western Australian Argon Isotope Facility, Curtin University of Technology, GPO Box U1987, Perth, WA 6845, Australia
[7]Department of Geoscience, University of Wisconsin-Madison, Madison, Wisconsin 53706, USA
[*]Corresponding author. E-mail: nadia.van.roosbroek@ulb.ac.be

(Received 04 September 2014; revision accepted 02 April 2015)

Abstract–A 435 kg piece of the Mont Dieu iron meteorite (MD) contains cm-sized silicate inclusions. Based on the concentration of Ni, Ga, Ge, and Ir (8.59 ± 0.32 wt%, 25.4 ± 0.9 ppm, 61 ± 2 ppm, 7.1 ± 0.4 ppm, respectively) in the metal host, this piece can be classified as a IIE nonmagmatic iron. The silicate inclusions possess a chondritic mineralogy and relict chondrules occur throughout the inclusions. Major element analysis, oxygen isotopic analysis ($\Delta^{17}O = 0.71 \pm 0.02‰$), and mean Fa and Fs molar contents ($Fa_{15.7 \pm 0.4}$ and $Fs_{14.4 \pm 0.5}$) indicate that MD originated as an H chondrite. Because of strong similarities with Netschaëvo IIE, MD can be classified in the most primitive subgroup of the IIE sequence. $^{40}Ar/^{39}Ar$ ages of 4536 ± 59 Ma and 4494 ± 95 Ma obtained on pyroxene and plagioclase inclusions show that MD belongs to the old (~4.5 Ga) group of IIE iron meteorites and that it has not been perturbed by any subsequent heating event following its formation. The primitive character of MD sheds light on the nature of its formation process, its thermal history, and the evolution of its parent body.

INTRODUCTION

Iron meteorites can be divided into magmatic (IC, IIAB, IIC, IID, IIIAB, IIIE, IIIF, IVA, and IVB) and nonmagmatic groups (IAB, IIICD, and IIE) based on chemical trends (Wasson and Wang 1986). The magmatic irons rarely contain silicate inclusions and their behavior on the siderophile elements versus Ni or Au plots is consistent with fractional crystallization of slowly cooling metallic liquids (Scott 1972; Choi et al. 1995). The nonmagmatic iron meteorites (NMIM) contain silicate inclusions of various nature and show trends on these elemental plots that cannot be explained by fractional crystallization alone (Scott 1972; Choi et al. 1995; Goldstein et al. 2009).

Within the nonmagmatic groups, a distinction is made between IAB–IIICD and IIE iron meteorites. IAB and IIICD irons are considered as an IAB iron-meteorite complex, consisting of a main group, five subgroups, and several grouplets (Wasson and Kallemeyn 2002). The IIE group can be distinguished from IAB and IIICD by the following characteristics (1) a much smaller Ni range (7.2–9.5 wt% for IIE versus 6–60 wt% for IAB-IIICD), (2) higher slopes on As-Ni and Au-Ni diagrams, (3) the absence of carbides, and (4) smaller fractions of FeS (Wasson and Wang 1986; Choi

© The Meteoritical Society, 2015.

et al. 1995). Apart from these characteristics, IIE irons also possess a wide variety of silicate inclusions, ranging from large chondritic clasts to smaller molten feldspar-rich globules (Ruzicka 2014).

The silicate-bearing IIE meteorites can be classified from primitive (1) to differentiated (5) on the basis of the nature of their silicates, according to the following sequence (1) Netschaëvo; (2) Techado; (3) Watson; (4) Miles and Weekeroo Station; and (5) Kodaikanal, Colomera, and Elga (Mittlefehldt et al. 1998). Netschaëvo is the most primitive member and contains preserved chondrules (Bunch et al. 1970; Bild and Wasson 1977).

Based on radioisotopic ages, the silicate-bearing IIE meteorites can be divided into two groups. Meteorites belonging to the "old group" (Weekeroo Station, Colomera, Miles, and Techado) have formation ages of ~4.5 Ga while the members of the "young group" (Netschaëvo, Kodaikanal, and Watson) have formation ages around 3.6 Ga (Bogard et al. 2000). This grouping by age does not coincide with the subdivision based on the mineralogical composition of the silicate inclusions.

Based on the silicate inclusions in these IIE meteorites, some authors suggested a direct link between the IIE NMIM and H chondrites (Olsen et al. 1994; Casanova et al. 1995; Gaffey and Gilbert 1998). The strongest arguments for this link are the similar oxygen isotope compositions (Clayton and Mayeda 1996), the presence of chondrules in Netschaëvo (Bunch et al. 1970; Bild and Wasson 1977), and an unmelted H chondrite inclusion found in Techado (Casanova et al. 1995). However, other authors question this link, and prefer a related, H chondrite like parent body, instead of the main H chondrite asteroid (Bogard et al. 2000). Bild and Wasson (1977) argued for derivation of the IIE irons from an HH chondrite body, more iron rich than the H chondrites that is supported by siderophile element abundances in the metal of IIE irons (Wasson and Wang 1986).

Based on the characteristics of the IIE silicate inclusions, several formation models have been proposed. These range from impact models (Burnett and Wasserburg 1967; Bence and Burnett 1969; Scott and Wasson 1976; Osadchii et al. 1981; Rubin et al. 1986; Wasson and Wang 1986; Olsen et al. 1994; Ikeda and Prinz 1996; Ikeda et al. 1997) or interior formation models (Wasserburg et al. 1968; Prinz et al. 1982; McCoy 1995) to a combination of both models (Bunch et al. 1970; Armstrong et al. 1990; Casanova et al. 1995; Ruzicka et al. 1999; Bogard et al. 2000; Hsu 2003; Takeda et al. 2003; Ruzicka and Hutson 2010), with or without links to the H chondrite parent body. More recently, the silicates in the IIE meteorites have been suggested to form by nebular processes (Kurat et al. 2007). To date, none of these models convincingly explains the diversity of features observed in the silicate inclusions from both differentiated and primitive IIE members.

Here, we present a detailed study of a large piece of the Mont Dieu meteorite (MD), a new member of the IIE group. This meteorite with a mass of 435 kg was found in 2005 in Sedan, France. This large piece is related to several fragments that were found in 1994 in the same geographic region, called the "Mont Dieu meteorites." Preliminarily classified as IIE nonmagmatic iron meteorites (Desrousseaux et al. 1996), the "Mont Dieu meteorites," showing intense and extensive rust damage, are preserved at the Musée National d'Histoire Naturelle in Paris. Except for the outer layer, this 435 kg piece is in a good state of preservation due to its large size and is now exhibited at the Royal Belgian Institute of Natural Sciences (RBINS) in Brussels, Belgium (Fig. 1a), and therefore will further be addressed as "the RBINS MD piece." A 1 cm-thick slice was cut from the middle of the RBINS MD piece, where several large, brownish silicate inclusions are present in the iron mass (Fig. 1b). These inclusions, crosscut by several parallel cracks, are angular and irregular, and the three largest inclusions have dimensions of 5 × 2 cm, 7 × 2 cm, and 5.5 × 2 cm. Abundant, round mm-sized troilite inclusions are also present in the iron matrix (Fig. 1c).

This study focuses mainly on the silicate inclusions, which are well preserved and of pristine nature. Therefore, they represent a unique opportunity to study the formation process(es) of the IIE NMIM and their enigmatic silicates.

ANALYTICAL TECHNIQUES

Metal Phase (LA-ICP-MS)

Three small metal fragments from the RBINS MD piece were mounted in epoxy and polished for laser ablation–inductively coupled plasma–mass spectrometry (LA-ICP-MS). A polished section previously Au-coated was also analyzed. Laser ablation measurements were performed with an ESI New Wave Research UP193FX excimer laser ablation system coupled to a Thermo Element XR magnetic sector-field ICP-MS unit at the Plasma Analytical Facility at Florida State University (Humayun 2012). Each of the three MD metal fragments was analyzed with a raster covering an area of 750 μm × 750 μm per fragment, and the polished section was rastered over a 1170 μm × 1170 mm area. The samples were scanned at 25 μm s^{-1} with a 50 μm beam spot, using a 50 Hz repetition rate. Four spot analyses were performed on two troilite inclusions and

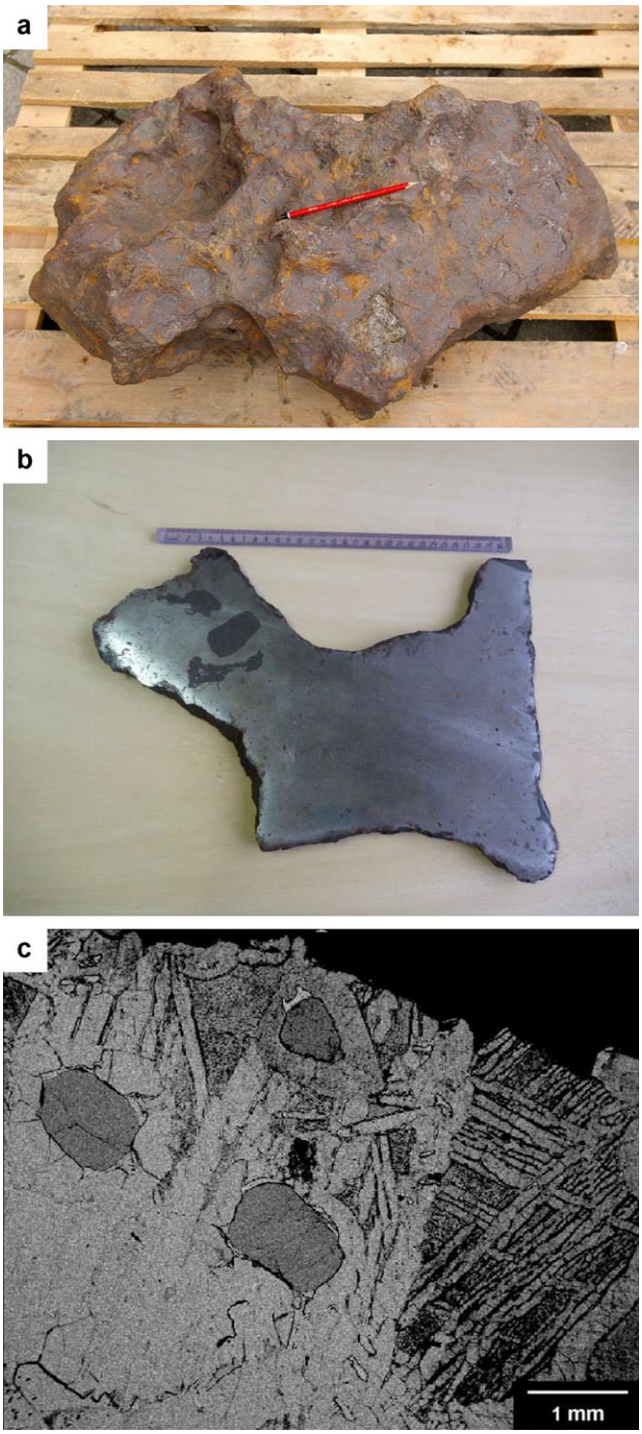

Fig. 1. Images of MD. a) The recovered RBINS MD piece of 435 kg. b) Slice cut from the RBINS MD piece, showing the distribution of the silicate inclusions. Length of ruler is 30 cm. c) BSE-SEM image of the metal host showing the Widmanstätten pattern (right) and round troilite inclusions.

two phosphide blebs, with a 50 μm beam spot and 20 s laser dwell time per spot. Peaks for ^{29}Si, ^{31}P, ^{34}S, ^{53}Cr, ^{57}Fe, ^{59}Co, ^{60}Ni, ^{63}Cu, ^{71} Ga, ^{74}Ge, ^{75}As, ^{95}Mo, ^{102}Ru, ^{103}Rh, ^{106}Pd, ^{120}Sn, ^{121}Sb, ^{182}W, ^{185}Re, ^{190}Os, ^{193}Ir, ^{195}Pt, and ^{197}Au were monitored in low resolution mode. Intensities were converted to elemental abundances using relative sensitivity factors (Humayun et al. 2007) determined on National Institute of Standards and Technology (NIST) SRM 610 silicate glass, NIST SRM 1263a steel and the iron meteorites North Chile (IIA) and Hoba (IVB) with abundances drawn from Wasson et al. (1989), Campbell et al. (2002), and Walker et al. (2008). The precision of the data can be judged from the relative standard deviation of the measurements, and is on the order of a few percent for most elements. No Au abundances are reported for the MD polished section because residual Au from the coating was detected in the raster. Results are presented in Table 1.

Silicate Phase

SEM and EMPA

Six polished sections, prepared from two different large silicate inclusions, were examined in detail. These large inclusions were situated at the outer part of the RBINS MD meteorite, where it was easy to sample during the sawing process. Backscattered electron imaging was performed at the Vrije Universiteit Brussel (VUB) using a JEOL JSM-6400 scanning electron microscope (SEM) with a Thermo Pioneer Si-Li detector with a resolution of 138 eV, and an accelerating voltage of 20 keV. Images were processed using the Thermo type NSS3 build 116 software. Modal abundances were defined using ImageJ free software. Eight representative high resolution BSE images covering areas of ~0.25 mm^2, 0.35 mm^2, 0.5 mm^2, 1 mm^2, 3 times 2 mm^2, and 5 mm^2 were selected for image analysis. The volume percentage of selected phases was calculated from the area distribution in the analyzed images, following a revised version of the technique described by Heilbronner (2000). Image processing was necessary for selection of the different phases. The modes obtained can be considered as representative of the real volume distribution by stereological assumptions (Underwood 1970).

Quantitative electron microprobe analysis (EMPA) was performed using a JEOL JXA-8500F electron microprobe at the Museum für Naturkunde Berlin. This microprobe is equipped with a field emission cathode, five wavelength dispersive spectrometers, and an energy-dispersive spectrometer. Measurement conditions for wavelength dispersive X-ray spectrometry (WDX) varied depending on properties and compositions of analyzed materials. Olivine and pyroxene were analyzed using 15 kV acceleration voltage, 15 nA beam current, and a beam defocused to 1 μm. Counting times were

Table 1. Siderophile element abundances (in μg g^{-1}) in metal from MD.

	Area 1	Area 2	Area 3	Polished section	**MD**	**±2 σ**	Troilite	Troilite	Phosphide	Phosphide
P	4200	2100	4500	4200	**3800**	**2200**	29	30	76500	156000
S	220	364	215	159	**240**	**175**	439000	437000	1600	1600
V	*1*	*1*	*1*	*1*	***1***		42	42	*2*	*2*
Cr	7	6	5	15	**8**	**9**	4780	3610	69	51
Mn	*1*	*1*	*1*	*1*	***1***		669	665	*2*	*1*
Fe	902000	907000	903000	905000	**904000**	**5000**	554000	557000	771000	602000
Co	4540	4540	4500	4500	**4520**	**50**	2	5	3470	1860
Ni	87300	84600	87100	84300	**85800**	**3200**	234	318	145000	237000
Cu	275	269	271	282	**274**	**12**	78	47	242	299
Ga	24.7	25.3	25.7	25.7	**25.4**	**0.9**	*0.03*	*0.03*	15.6	7.2
Ge	60	60	62	62	**61**	**2**	1	1	43	18
As	10.2	9.6	9.9	10.6	**10.1**	**0.9**	*0.03*	*0.03*	9.4	5.3
Mo	6.02	5.87	6.32	6.21	**6.10**	**0.39**	4.96	3.93	18.7	33.7
Ru	10.20	9.87	10.05	10.41	**10.13**	**0.46**	*0.02*	*0.02*	11.4	14.4
Rh	1.45	1.40	1.44	1.48	**1.44**	**0.07**	0.007	*0.005*	1.44	1.28
Pd	3.44	3.33	3.38	3.44	**3.40**	**0.10**	*0.017*	*0.018*	3.39	4.01
Sn	0.48	0.51	0.48	0.53	**0.50**	**0.05**	*0.1*	*0.1*	*0.5*	*0.4*
Sb	0.24	0.19	0.20	0.23	**0.21**	**0.05**	*0.01*	0.03	0.09	0.10
W	1.23	1.18	1.18	1.28	**1.22**	**0.09**	*0.001*	0.002	1.05	0.94
Re	0.72	0.70	0.68	0.75	**0.71**	**0.06**	*0.0005*	*0.0005*	0.64	0.23
Os	7.63	7.58	7.31	7.97	**7.62**	**0.54**	*0.002*	*0.002*	5.91	2.19
Ir	7.19	7.12	6.88	7.37	**7.14**	**0.41**	*0.001*	*0.001*	5.54	2.00
Pt	13.2	12.8	12.9	13.4	**13.1**	**0.5**	*0.008*	*0.008*	9.4	3.5
Au	0.94	0.92	0.94		**0.93**	**0.03**				

Siderophile element abundances are in μg g^{-1} from raster analyses and spot analyses of two troilite and two schreibersite inclusions in MD. Average and 2σ standard deviation are shown in bold. Abundances below detection limits are italicized.

20 s on the peak and 10 s on the background on all major elements except for Na and K where half of the counting times were used to minimize effects of alkali-loss during measurements on plagioclase. Standardization was performed using international Smithsonian and Astimex natural mineral standards.

Raman Spectroscopy

Raman spectroscopy was carried out at the VUB using a LabRAM HR Evolution (HORIBA Scientific) confocal Raman spectrometer and the LabSpec software. This instrument is equipped with a high stability confocal microscope with XYZ motorized stage, 10×, 50×, 100× – 50× (WD = 10.6 mm) objectives and a multichannel air-cooled CCD detector (spectral resolution <1 cm^{-1}, lateral resolution 0.5 μm, axial resolution 2 μm). Raman spectra were excited with a solid-state green laser (532 nm wavelength; ~6.25 mW power).

ICP-OES and ICP-MS

For bulk major and trace analyses, a fragment of the investigated silicate inclusions of MD was washed with acetone and chips showing visible rust were carefully removed. Next, the fragment was crushed using an agate mortar and pestle to obtain a fine homogeneous powder. This powder (1.102 g) was calcined in the furnace overnight at 500 °C. A net gain of 2.3% by weight was observed, due to the conversion of Fe^0 to Fe^{2+} and Fe^{2+} to Fe^{3+}.

For the major element analysis, about 25 mg of MD and the three standards, PCC-1 (peridotite, United States Geological Survey, USGS), BR (basalt, Centre de Recherches Petrographiques et Geochimiques, Nancy), and BCR-2 (basalt, USGS) were used. The powder was mixed with approximately 125 mg of $LiBO_2/Li_2B_4O_7$ and fluxed in graphite crucibles by heating for 15 min in a muffle furnace at ~1000 °C. The resulting melt was dissolved in 50 mL 0.40 M HNO_3 using a magnetic stirrer for 10–15 min. Finally, 10 mL of each solution was diluted with 15 mL of 0.40 M HNO_3. The major element analysis was performed using a VARIAN 720 ES inductively coupled plasma–optical emission spectrometer (ICP-OES) at the Katholieke Universiteit Leuven (KUL). Total reproducibility is estimated to be better than 5%. (Results will be presented in Table 4.)

For the trace element analysis, about 25 mg of MD silicate and of the reference material BCR-2 were accurately weighed. Each sample was mixed with 2.5 mL concentrated HF, 2.5 mL concentrated HCl, and 2 mL concentrated HNO_3 in Savillex PFA beakers.

Table 2. Modal composition (area%) of MD determined by image processing using the ImageJ free software, compared to average H chondrite (vol%) (Ruzicka et al. 2005).

	Mont Dieu IIE	H Ordinary chondrites
Olivine	33	38.09
Low-Ca pyroxene	30	29.47
High-Ca pyroxene	–	4.76
Plagioclase	7	13.59
Phosphate	2	0.71
Chromite	1	0.57
Ilmenite	–	0.18
Troilite	22	4.25
Fe-Ni metal	5	8.21

The area% defined for MD by image analysis is considered representative to the volume distribution (Underwood 1970).

After evaporation of the samples, some precipitate was still present. Therefore, 1.5 mL HCl was added and evaporated again. Each sample was mixed with 1 mL $HClO_4$ and 4 mL HNO_3, indium (In) was added as an internal standard, and the solutions were evaporated. After appropriate dilution, the solutions were analyzed at Ghent University (UGent), with a Thermo Fisher Scientific Element XR sector-field ICP-MS unit. Total reproducibility is generally better than 5%. (Results will be presented in Table 5.)

LA-ICP-MS

Because the bulk REE concentrations of the silicate fraction were determined using a small amount of material, phosphates might not have been representatively sampled, as these make up only 2 area% of the investigated inclusions (Table 2) and are heterogeneously distributed throughout the inclusions. To address this issue, REE concentrations in merrillite and apatite were analyzed in situ using LA-ICP-MS. These analyses were performed using a Teledyne Cetac Technologies Analyte G2 excimer-based laser ablation system equipped with a standard 10 cm × 10 cm Helex ablation cell and coupled to a Thermo Scientific Element XR double-focusing sector field ICP-mass spectrometer at the Department of Analytical Chemistry at Ghent University, following the procedure described in Martin et al. (2013). Using a repetition rate of 30 Hz, each phosphate was ablated for 15 s using a laser spot size of 50 μm. The mineralogy was verified by monitoring the signal intensities of Mg, Si, Cr, and Fe. Quantification was achieved through external calibration against seven certified glass reference standards USGS-BCR-2G, USGS BHVO-2G, USGS BIR-1G, USGS GSD-1G, USGS GSE-1G, NIST SRM 610, and NIST SRM 612. Based on the standards, reproducibility for the reported elements is better than 5% RSD. (LA-ICP-MS trace element data of merrillite and apatite in MD will be presented in Fig. 5.)

Oxygen Isotope Analysis

For the oxygen isotope analysis, a silicate fragment of MD, from one of the inclusions, was washed with acetone and again chips showing rust were carefully removed. This piece was gently crushed using an agate mortar and pestle. The sample was then sieved with two stacked sieves of 150 μm and 250 μm. The 150–250 μm fractions were used to perform a heavy liquid mineral separation, using methylene iodide (3.3 g cm^{-3}). The purified silicate fraction ($D < 3.3$) was analyzed for oxygen three isotopes at the University of Wisconsin-Madison (USA) using a CO_2 laser and BrF_5 as the fluorinating agent. Oxygen gas was purified by cryogenic methods and with hot Hg, and measured as O_2 to facilitate the determination of $\delta^{17}O$. The measured $\delta^{17}O$ and $\delta^{18}O$ values were corrected based on multiple analysis of UWG-2 garnet standard (Valley et al. 1995) and the $\Delta^{17}O$ was calculated relative to UWG-2 following the method outlined in Spicuzza et al. (2007).

$^{40}Ar/^{39}Ar$ Analysis

We separated unaltered, optically transparent, <<150 μm-size crystals of plagioclase (5) and pyroxene (10). These minerals were carefully hand-picked under a binocular microscope. The minerals were thoroughly rinsed with distilled water.

Samples were loaded into 2 large wells of one 1.9 cm diameter and 0.3 cm depth aluminum disk. These wells were bracketed by small wells that included Hb3gr hornblende used as a neutron fluence monitor for which an age of 1081.0 ± 1.0 Ma (1σ) was adopted (Renne et al. 2011) and a good in-between-grains reproducibility has been demonstrated (Jourdan et al. 2006; Jourdan and Renne 2007). The disks were Cd-shielded (to minimize undesirable nuclear interference reactions) irradiated for 40 h in the US Geological Survey nuclear reactor (Denver, USA) in central position. The mean J-value computed from standard grains of the disk is 0.008215 ± 0.0000156 determined as the average and standard deviation of J-values of the small wells for each irradiation disk. Mass discrimination was monitored using an automated air pipette and provided a mean value of 1.005413 (±0.36%) per dalton (atomic mass unit) relative to an air ratio of 298.56 ± 0.31 (Lee et al. 2006). The correction factors for interfering isotopes were $(^{39}Ar/^{37}Ar)_{Ca} = 7.06 \times 10^{-4}$ (±7%), $(^{36}Ar/^{37}Ar)_{Ca} = 2.81 \times 10^{-4}$ (±3%) and $(^{40}Ar/^{39}Ar)_K = 0.76 \times 10^{-4}$ (±10%) (Cosca et al. 2011).

The $^{40}Ar/^{39}Ar$ analyses were performed at the Western Australian Argon Isotope Facility at Curtin University. Single plagioclase grains were analyzed without any wrapping. Multigrain pyroxene crystals were wrapped in zero-blank niobium foil. Samples were step-heated using a 110 W Spectron Laser Systems, with a continuous Nd-YAG (IR; 1064 nm) laser rastered over the sample during 1 min to ensure a homogenously distributed temperature. The gas was purified in a stainless steel extraction line using an AP10 SAES getter. Ar isotopes were measured in static mode using a MAP 215-50 mass spectrometer (resolution of ~450; sensitivity of 4×10^{-14} mol V^{-1}) with a Balzers SEV 217 electron multiplier using 9–10 cycles of peak-hopping. The data acquisition was performed with the Argus program written by M. O. McWilliams and ran under a LabView environment. The raw data were processed using the ArArCALC software (Koppers 2002) and the ages have been calculated using the decay constants recommended by Renne et al. (2011). Blanks were monitored every 3–4 steps and typical ^{40}Ar blanks range from 1×10^{-16} to 2×10^{-16} mol. Ar isotopic data corrected for blank, mass discrimination and radioactive decay are given in Annex S1 of supporting information. Individual errors in Annex S1 are given at the 1σ level. Our criteria for the determination of plateau are as follows: plateaus must include at least 70% of ^{39}Ar. The plateau should be distributed over a minimum of three consecutive steps agreeing at 95% confidence level and satisfying a probability of fit (P) of at least 0.05. Plateau ages (Figs. 8 and 10) are given at the 2σ level and are calculated using the mean of all the plateau steps, each weighted by the inverse variance of their individual analytical error. All sources of uncertainties are included in the calculation.

RESULTS

Metal Host

The metal phase clearly shows Widmanstätten pattern (WP) with wider kamacite lamellae (0.3 mm) and finer taenite lamellae. This allows the RBINS MD piece to be classified as a fine octahedrite (Buchwald 1975). Troilite is widespread throughout the Fe-Ni host, often associated with schreibersite (Fig. 1c). Compositional results for the metal phase obtained by LA-ICP-MS are given in Table 1. The bulk metal phase contains 4520 ± 50 ppm of Co, 8.59 ± 0.32 wt% of Ni, 25.4 ± 0.9 ppm of Ga, 61 ± 2 ppm of Ge, 10.1 ± 0.9 ppm of As, 7.1 ± 0.4 ppm of Ir, and 0.93 ± 0.03 ppm of Au (uncertainties reported as 2σ). The Co, Ga, Ge, and As abundances agree well with previously reported results by instrumental neutron activation analysis (INAA) for Mont Dieu (Desrousseaux et al. 1996), but the Ni (+17%), Ir (+39%), and Au (+14%) abundances are higher in the RBINS MD piece than those reported previously for other Mont Dieu fragments (Desrousseaux et al. 1996). To explore the effect of kamacite-taenite sampling, we examined the distribution of elemental abundances relative to variations in the Ni abundance within each raster, but found that nowhere could we attain 4.9 ppm of Ir as reported by INAA (Desrousseaux et al. 1996). Further, Desrousseaux et al. (1996) reported a Ni abundance of 8.6 wt% from their SEM-EDS measurement for Mont Dieu, which is within error of the value we obtained by LA-ICP-MS. Small discrepancies between the LA-ICP-MS data and bulk INAA are expected since the LA-ICP-MS measurements were performed on metal, avoiding troilite or schreibersite inclusions. These data agree best with the concentrations reported for IIE NMIM with Ni, Ga, Ge, and Ir concentration ranges of 7.2–9.5 wt%, 21–28 ppm, 62–75 ppm, and 1–8 ppm, respectively (Wasson 1985; Wasson and Wang 1986), and link the RBINS MD piece to the Mont Dieu fragments recovered in 1994 (Desrousseaux et al. 1996; Grossman 1997). Based on these observations, the RBINS MD piece can be assigned to the IIE group.

Silicate Inclusions

Texture and Mineral Chemistry

The six examined polished sections of silicate inclusions are mostly characterized by a recrystallized coarse-grained texture cut by metal and troilite veins. The mineralogy consists of olivine, low-Ca pyroxene, plagioclase, Fe-Ni metal, sulfide, phosphates, and chromite. Modal abundances are given in Table 2. Within the silicate-rich inclusions, well-defined round structures with diameters ranging between 400 μm and 1.5 mm, and averaging ~1 mm, are present (Figs. 2c and 2e–g). These structures, mainly composed of low-Ca pyroxene and olivine with interstitial plagioclase, are interpreted to represent relicts of chondrules. Raman spectroscopy confirms the presence of crystalline plagioclase. No glass has been preserved in the chondrules. A total of 13 relict chondrules were identified in one of the silicate inclusions of MD. Seven of these relict chondrules are well preserved in the silicate inclusion and can directly be compared to chondrules found in chondrites. Six are barred olivine chondrules (Figs. 2c and 2f), and one is a porphyritic pyroxene chondrule (Fig. 2e). The other appears to have recrystallized (Fig. 2g). Several other textures present in the silicate inclusions could be interpreted as relicts of chondrules, but these are not as obvious as the

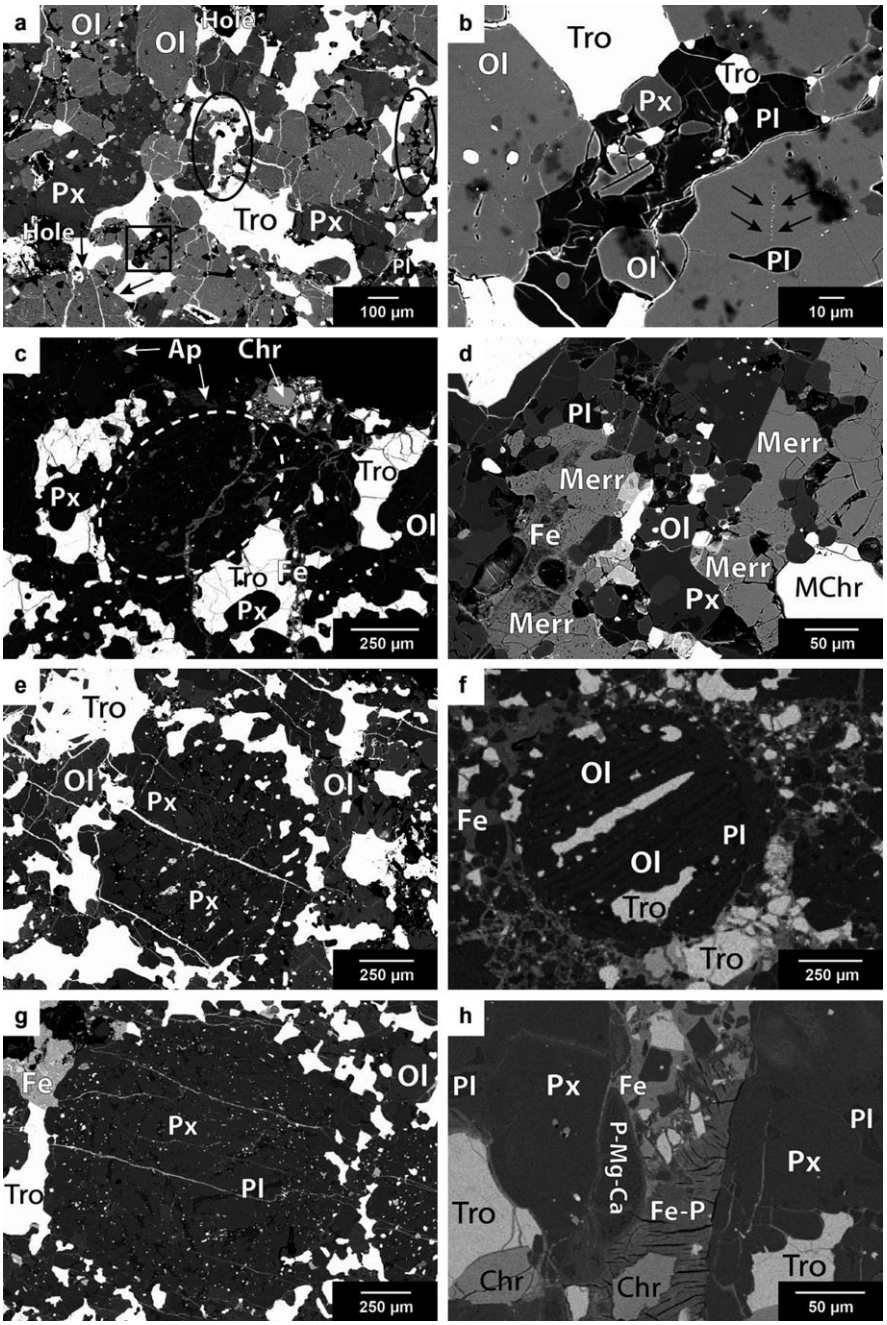

Fig. 2. Petrographic features of MD silicate. a) Matrix area showing the distribution of elongated, irregular grains of troilite (Tro), coarse-grained olivine (Ol), and pyroxene (Px) with interstitial plagioclase (Pl). Fine-grained regions are highlighted with ellipses, porous olivine in left corner (arrows). b) Zoom of the area indicated with a box in image (a), large plagioclase with inclusions. Trails of tiny troilite blebs are present in surrounding pyroxene and olivine (arrows). c) BO chondrule (circle), showing the distribution of Fe-Ni (Fe), troilite, apatite (Ap), and chromite (Chr) phases. The network of Fe veins and patches is connected to coarse-grained troilite that can be porous (left corner). Small blebs of Fe-Ni and troilite are widespread in the silicate portion. d) Matrix area showing coarse-grained intergrowths of merrillite (Merr) with Fe-P. In between the two phosphate patches, a fine-grained assemblage of rounded grains of olivine, plagioclase, and troilite is present. A magnesiochromite (MChr) grain is present in the right corner. e) Porphyritic pyroxene chondrule with interstitial plagioclase and a rim of irregular troilite patches, with offshoots resulting in veins crossing the chondrule and surrounding silicates. f) BO chondrule with interstitial plagioclase and large elongated grains of troilite. The network of Fe-Ni forms a rim around the chondrule. g) Recrystallized chondrule mainly consisting of pyroxene with intersitital plagioclase. Olivine is predominantly present as smaller round inclusions in larger pyroxene grains at the edge. An Fe-troilite intergrowth is present in the left corner. h) Part of one of the thick veins crossing the inclusion. At the left edge of the vein, a porous phase consisting of P-Mg-Ca-Na with a rim of Fe-P is present. All images are BSE-SEM.

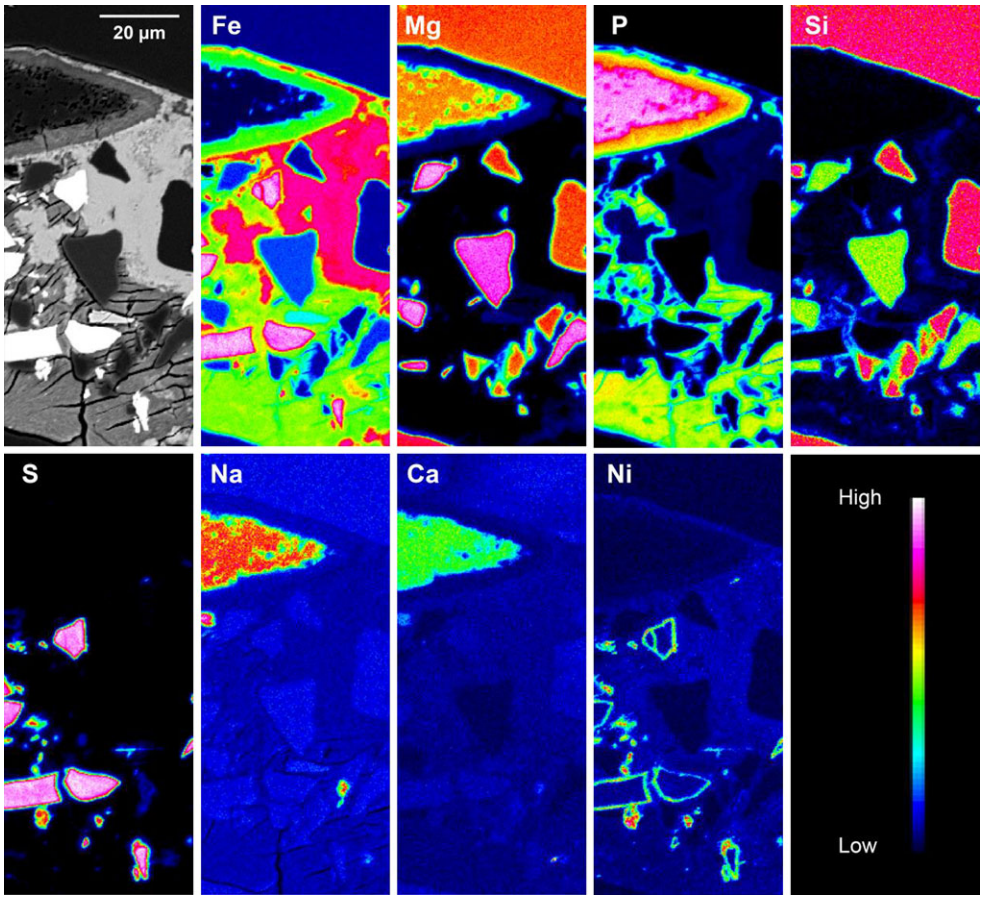

Fig. 3. X-ray elemental mapping of a part of the thick vein in MD silicate. a) BSE image of the area. b) Fe-map showing the groundmass of the vein, and the rim around the porous phase at the border. c) Mg-map showing the pyroxene next to the vein and its presence in the porous phase. d) P-map showing its distribution in the groundmass of the vein and its zoning in the porous phase. e) Si-map showing the distribution of the silicate clasts. f) S-map showing the distribution of the troilite clasts and its absence in the groundmass. g) Na-map showing its presence in the inner part of the porous phase. h) Ca-map showing its presence in the inner part of the porous phase. i) Ni-map showing its presence as rims around troilite grains. Color scale bar indicates relative X-ray intensities from low to high.

identified features. Nevertheless, these relicts support the widespread occurrence of chondrules in the silicate inclusions of MD.

Two types of veins crosscut the silicate inclusions: fine veinlets crossing the chondrules and the matrix and, less abundant, subparallel thick veins that pass through the entire inclusion. The fine veinlets consist of a groundmass composed of a mixture of Fe-Ni-P and troilite connecting large troilite and metal patches throughout the inclusion, and crosscutting silicate minerals (Figs. 2a, 2c, 2e, and 2g). The veinlet width varies between 1 μm and 10 μm, and the wider of these veins contain small (<5 μm) angular clasts of olivine, pyroxene, plagioclase, and troilite (Fig. 2c). These veining textures are much more pronounced in the matrix and the smallest chondrules than in the larger chondrules.

The subparallel thick veins are heterogeneously distributed throughout the inclusions and are about 100–200 μm wide (Figs. 2h and 3). The matrix of these veins is composed of Fe-Ni and Fe-P (Fig. 3), and is locally filled with angular and subrounded clasts of olivine ($Fa_{17.5 \pm 0.4}$), pyroxene ($Fs_{14.8 \pm 0.5}$), plagioclase ($Ab_{83.7 \pm 1.3}$ $An_{11.9 \pm 1.7}$ $Or_{4.5 \pm 0.9}$), and troilite with a random grain size distribution ranging from <5 μm to 100 μm (Fig. 2h). About half of the surface of the vein is free of clasts. At the margin of the veins, a rounded elongated porous, likely amorphous, domain of P-Mg-Ca-Na occurs locally, with a rim of Fe-P (Fig. 3). The veins locally have thinner offshoots that can result in patches of Fe-Ni-P filled with small (<10 μm) clasts of silicates and troilite. These patches are connected to the veinlets and, as such, the two types of veins form a network within the inclusions (Fig. 2c).

The silicate minerals display an interlocking texture dominated by pyroxene and olivine with interstitial

Table 3. Mean composition and standard deviation of the mean of silicate minerals in MD (matrix and chondrules) (wt%) determined by electron microprobe analysis.

	Olivine	Low-Ca pyroxene	Plagioclase
SiO_2	39.6 ± 0.3	56.3 ± 0.4	65.0 ± 1.0
TiO_2	<0.02	0.2 ± 0.1	0.1 ± 0.02
Al_2O_3	0.1 ± 0.05	0.3 ± 0.1	20.8 ± 0.6
Cr_2O_3	<0.04	0.2 ± 0.1	0.02 ± 0.02
FeO	15.2 ± 0.4	9.5 ± 0.3	0.9 ± 0.4
MnO	0.4 ± 0.03	0.4 ± 0.03	0.02 ± 0.02
MgO	45.6 ± 0.4	32.4 ± 0.5	0.5 ± 0.2
CaO	<0.02	0.9 ± 0.3	2.5 ± 0.6
Na_2O	<0.03	0.04 ± 0.02	9.4 ± 0.3
K_2O	<0.01	<0.01	0.7 ± 0.2
Total	101.0	100.2	100.0
End member	$Fa_{15.7 \pm 0.4}$	$Fs_{14.4 \pm 0.5}Wo_{1.7 \pm 0.6}$	$Ab_{83.5 \pm 2.0}Or_{4.3 \pm 1.2}$
N	80	84	92

N = number of analyses averaged.

plagioclase (Fig. 2a). Grain sizes and textures vary throughout the inclusions. The silicate portion is often composed of subeuhedral grains of olivine and pyroxene varying between 100 and 500 μm, with smaller irregular plagioclase patches ranging from 10 to 50 μm in between (Fig. 2a). Less commonly, in association with large troilite and metal patches (~300–700 μm), plagioclase grains up to 150 μm occur, containing and surrounded by round olivine, pyroxene, and troilite grains of about 10–20 μm in diameter (Fig. 1b). These features are not only present at the edge of the chondrules but are also widespread throughout the matrix. Fine-grained assemblages are also present, consisting mainly of interlocking round grains of pyroxene and olivine, often accompanied by rounded grains of troilite and plagioclase, and to a lesser extent metal (Figs. 2a and 2d). These regions have grain sizes of about 10–20 μm. Between and within the silicate grains, abundant round troilite blebs (<5–20 μm) are present (Figs. 2a and 2b). This feature is more pronounced in the matrix than in the chondrules. Plagioclase generally exhibits small (often <10 μm) round inclusions of olivine, pyroxene, troilite, or metal and is commonly crossed by troilite veinlets (Fig. 2b). Plagioclase is also present as round blebs of 5–20 μm within olivine and pyroxene grains, and smaller round grains of pyroxene and olivine are locally present in larger grains of olivine and pyroxene (Fig. 2a). A few grains of porous olivine are observed in the matrix (Fig. 2a).

The composition of olivine and low-Ca pyroxene is homogeneous within the chondrules and the matrix, with an average molar content of $Fa_{15.7 \pm 0.4}$ and $Fs_{14.4 \pm 0.5,}$ respectively (Table 3). This is roughly consistent with the compositions in average H chondrites, where Fa in olivine is in the range of 16–20 mole% and Fs in low-Ca pyroxene in the range of 14.5–18 mole% (Brearley and Jones 1998). MD appears slightly more reduced. All the plagioclase grains are albitic and the composition is homogeneous throughout the matrix and the chondrules ($Ab_{83.5 \pm 2.0}$ $An_{12.2 \pm 2.9}$ $Or_{4.3 \pm 1.2}$) (Table 3). This composition is in good agreement with the mean composition of plagioclase in average H chondrites ($Ab_{82}An_{12}Or_6$) (Brearley and Jones 1998). The homogeneity of olivine and pyroxene composition and the occurrence of crystalline plagioclase larger than 50 μm allow the determination of the general petrologic type of the investigated silicate inclusions as type 6 (Weisberg et al. 2006).

To define the shock stage of the inclusions, one thin polished section (30 μm thick) sampled from one of the inclusions was examined. The silicate minerals do not display any shock features such as undulatory extinction, fracturing, or mosaicism. Based on these observations, a shock stage S1 can be assigned to the silicate phase of MD, using the classification scheme for shock metamorphism (Stöffler et al. 1991).

Fe-Ni Metal

The majority of the Fe-Ni phase in the silicate inclusions is oxidized, likely due to terrestrial weathering. It is no longer possible to distinguish kamacite from taenite. The metal areas occur mostly in the matrix and around the chondrules and are characterized by an amoeboid appearance. Metal is mostly present in the form of intergrowths with troilite, generally forming a rim around troilite grains (Figs. 2c, 2f, and 2g), but it can also appear (1) as smaller round and elongated grains between silicate minerals (Fig. 2c); (2) associated with P, as intergrowths with phosphate minerals (Fig. 2d); (3) as the groundmass of the veinlets (Figs. 2c and 2g); and (4) as the matrix of the thick veins, together with an Fe-P phase (Fig. 2h).

Table 4. Major and trace element abundances for the silicate inclusions of MD, Netschaëvo, Watson, and major and trace element abundances for average H and L chondrites.

Meteorite Classification	Mont Dieu IIE	Netschaëvo IIE	Watson IIE	H Ordinary chondrites	L Ordinary chondrites
SiO_2	30.42	32.37	45.51	36.52	39.88
TiO_2	0.074	0.21	0.14	0.13	0.15
Al_2O_3	1.25	1.82	2.54	2.43	2.31
Cr_2O_3	0.92	0.59	0.49	0.36	0.44
Fe*	40.84	37.29	14.27	31.45	26.99
MnO	0.28	0.35	0.37	0.25	0.27
MgO	21.39	19.65	31.41	23.48	24.89
CaO	0.96	1.64	2.29	1.82	1.9
Na_2O	0.42	0.76	1.08	0.85	0.88
K_2O	0.13	0.19	0.28	0.14	0.14
P_2O_5	0.54	0.54	0.60	0.23	0.26
LOI	−2.3 [a]	1.18	0.018	0.43	0.43
Total	94.92	96.59	99.00	98.09	98.54
$Fe_2O_{3\ TOTAL}$	40.84[b]	48.58[c]	15.76[c]	39.35[c]	31.19[c]
V	89				
Co	154	1000	<100	800	600
Ni	2284	25000	1300	15800	11200
Zn	133				

Data for Netschaëvo, H, and L chondrites from Olsen and Jarosewich (1971), data for Watson from Olsen et al. (1994).
Oxides in wt%, trace elements in ppm. All elements (except S) for MD measured by ICP-OES (S was not determined).
Fe* for MD = $Fe_2O_{3\ TOTAL}$; Fe* for Netschaëvo, Watson, H, and L chondrites = FeO + FeS + Fe.
[a]In the case of MD, a gain of 2.3 wt% was observed after calcination, due to the conversion of $Fe^0 \rightarrow Fe^{2+}$ and $Fe^{2+} \rightarrow Fe^{3+}$.
[b]$Fe_2O_{3\ TOTAL}$ analyzed by ICP-OES.
[c]$Fe_2O_{3\ TOTAL}$ calculated from the data of Olsen and Jarosewich (1971) for Netschaëvo, H, and L chondrites and Olsen et al. (1994) for Watson.

Sulfide

Troilite is an abundant mineral in the MD silicate inclusions. It occurs in the following forms. (1) In the matrix as large coarse grains (up to 750 μm) commonly associated with Fe-Ni (Fig. 2c). These grains have an amoeboid and elongated appearance and flow through the inclusions crosscutting and enclosing silicate phases (Figs. 2a, 2c, 2e, and 2g). These large grains may appear porous and are crosscut by fractures that are filled with Fe-Ni, now oxidized (Figs. 2c and 2h). (2) Rimming chondrules (Figs. 2c and 2e–g). (3) In veinlets, locally filled with small silicate clasts that in some cases shoot off into small patches (Figs. 2a and 2e). (4) In abundant small blebs ranging from <5 μm to 20 μm within the silicate minerals in the matrix and the chondrules. These blebs can be randomly distributed in and around the silicate grains but also occur as trails in the grains (Figs. 2a and 2b).

Phosphates

Phosphates are present in the inclusions in the form of (chlor) apatite and merrillite minerals. These minerals generally have an amoeboid and occasionally porous appearance (Fig. 2d); are heterogeneously distributed around chondrules and throughout the matrix; and are interwoven with each other, and/or with the metal phase. Phosphates are generally coarse-grained ranging between 200 and 300 μm (Fig. 2d). Merrillite and apatite are chemically homogeneous and their mineral formulas are $(Ca_{2.605}Fe_{0.031}Mg_{0.287}Mn_{0.002}Na_{0.238})(PO_4)_2$ and $(Ca_{4.776}Fe_{0.057}Mn_{0.015}Na_{0.005}Si_{0.019})(PO_4)_3\ Cl_{0.907}$, respectively.

Chromite

Chromite, locally as magnesiochromite (Fig. 2d right corner), is a minor mineral phase in the inclusions, ranging in size from 10 to 100 μm. It occurs exclusively in the matrix, where it is heterogeneously distributed, and generally associated with troilite, metal, and/or phosphate (Figs. 2c, 2d, and 2h). Chromite grains are euhedral (Figs. 2c and 2h) and are compositionally homogeneous.

Major Element Analysis

The results of the major element analysis are listed in Table 4, together with the compositions of Netschaëvo (IIE), Watson (IIE), H, and L chondrites (Olsen and Jarosewich 1971; Olsen et al. 1994). Iron oxide (40.84 wt%) and SiO_2 (30.42 wt%) are the most abundant oxides in the silicate inclusions of MD, followed by MgO (21.39 wt%) and Al_2O_3 (1.25 wt%). Among the IIE members, Netschaëvo is most similar in

Table 5. CI-normalized (McDonough and Sun 1995) REE abundances for the silicate inclusions of MD (determined by ICP-MS analysis), the silicate inclusions of Netschaëvo, the silicate inclusions of Watson, H, EL chondrites, and reference material BHVO-2.

Element	Mont Dieu	Netschaëvo	Watson	H chondrites	EL chondrites	BHVO-2 (Martin et al. 2013)	Jochum and Stoll (2008)
La	0.64	0.85	1.76	1.26	0.81	15.5 ± 0.1	15.2
Ce	0.54	–	1.58	1.38	0.50	39.0 ± 0.6	37.6
Pr	0.56	–	–	1.38	–	5.49 ± 0.10	5.35
Nd	0.59	–	–	1.39	0.52	25.5 ± 0.77	24.5
Sm	0.73	1.09	1.48	1.26	0.92	6.34 ± 0.19	6.10
Eu	0.62	1.96	1.34	1.30	0.96	2.06 ± 0.01	2.07
Gd	0.64	–	–	1.52	0.54	6.25 ± 0.13	6.16
Tb	0.78	–	1.65	1.46	–	0.98 ± 0.03	0.92
Dy	0.86	–	1.61	1.41	0.57	5.55 ± 0.14	5.28
Yb	0.88	1.29	1.49	1.26	1.02	2.12 ± 0.06	2.01
Lu	0.92	1.03	1.67	1.28	0.99	0.29 ± 0.01	0.28

Values are given in μg g^{-1}. Data for Netschaëvo from Bild and Wasson (1977), for Watson from Olsen et al. (1994), and for H and EL chondrites from Wasson and Kallemeyn (1988).

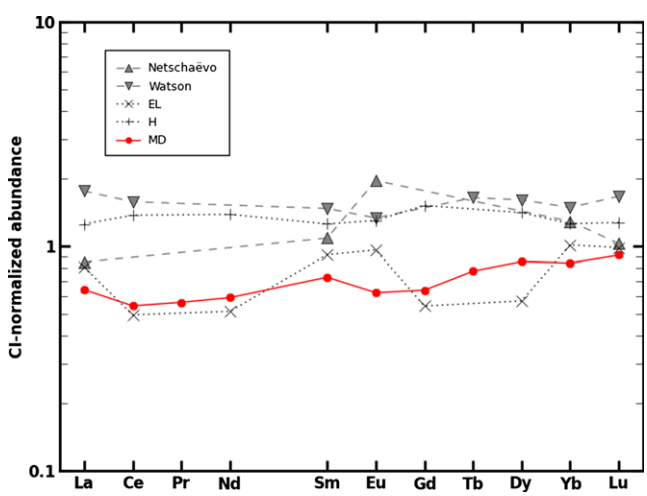

Fig. 4. CI-normalized (McDonough and Sun 1995) trace element abundances of the silicate inclusions of MD, Netschaëvo IIE, Watson IIE, H chondrites, and EL chondrites. Data for Netschaëvo from Bild and Wasson (1977), for Watson from Olsen et al. (1994), and for H and EL chondrites from Wasson and Kallemeyn (1988).

composition, with compositional differences of 6% for SiO_2, 8% for MgO, and 17% for Fe_2O_3. Because Fe is measured as Fe_2O_3 in MD and as FeO, FeS, and Fe metal in Netschaëvo, Watson, H, and L chondrites (Table 4), the total amount of Fe for these meteorites is recalculated as Fe_2O_3. The largest differences between MD and Netschaëvo are found for TiO_2, Na_2O, and CaO that differ by 95%, 57%, and 52%, respectively. In addition, the Ni content is 11 times higher in Netschaëvo. As no bulk major element analysis has been performed for Techado, its silicate fraction cannot be compared to MD. The compositional difference between Watson and MD is large, with most oxides showing a difference of >30%, including important oxides such as MgO, SiO_2, and Fe_2O_3 (Table 4). When comparing MD with chondrites, H chondrites show the best agreement, with a difference of 4%, 9%, and 18% for Fe_2O_3, MgO, and SiO_2 respectively (Table 4). The most important differences are in the amount of CaO, Na_2O, and Al_2O_3, which differ by approximately 60–70%. This difference is also reflected in the modal abundances (Table 2), with lower abundances of plagioclase and the absence of high-Ca pyroxene in MD. Also, Ni is five times more abundant in H chondrites than in MD silicates. Compared to L chondrites, the difference with MD is larger, mostly reflected in the MgO and SiO_2 and Fe_2O_3 content that differ by 15%, 27%, and 27%, respectively.

Trace Element Analysis

Figure 4 shows the CI-normalized rare earth elements (REE) pattern for the bulk silicate fraction of MD (Table 5), compared to the REE patterns determined for Netschaëvo, Watson, H, and EL chondrites. The pattern of MD is depleted compared to H chondrites and also more fractionated, especially in terms of the light rare earth elements (LREE). The $(La/Sm)_N$ and $(La/Yb)_N$ ratios are 0.88 and 0.73 respectively, while these values are ~1 for H chondrites (Olsen et al. 1994). In terms of REE, MD can best be compared to EL6 chondrites that have $(La/Sm)_N$ and $(La/Yb)_N$ ratios of 0.88 and 0.8 respectively, defined by Wasson and Kallemeyn (1988) and confirmed by Rubin et al. (2009) ($[La/Sm]_N = 0.89 \pm 0.07$; $[La/Yb]_N = 0.79 \pm 0.11$). For Netschaëvo, only a few REE concentrations were determined (La, Sm, Eu, Yb, and Lu). Note that Netschaëvo has a positive Eu anomaly implying excess plagioclase relative to a chondritic

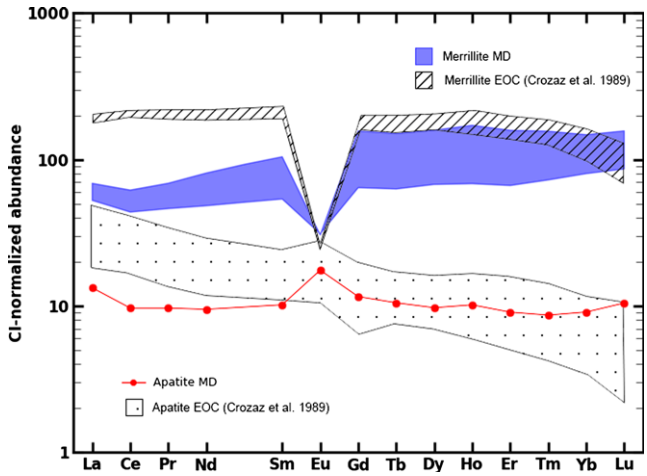

Fig. 5. CI-normalized (McDonough and Sun 1995) trace element abundances of merrillite and apatite in the silicate inclusions of MD, compared with the trace element abundances of these minerals in equilibrated ordinary chondrites (EOC; Crozaz et al. 1989).

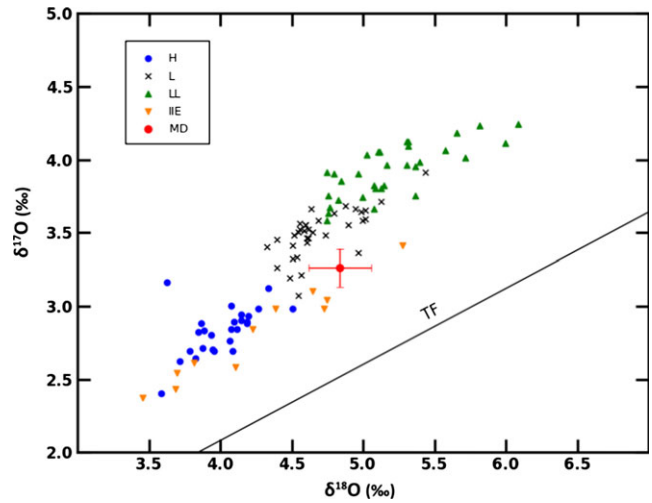

Fig. 6. Oxygen isotope compositions of the silicate inclusions of MD compared with ordinary chondrites and silicate inclusions of other IIE irons. The equation for the terrestrial fractionation line (TF) is $\delta^{17}O = 0.52 * \delta^{18}O$. Data for IIE irons from Clayton and Mayeda (1996), and for ordinary chondrites from Clayton et al. (1991).

source. These REE are also depleted compared to H chondrites and have $(La/Sm)_N$ and $(La/Yb)_N$ ratios of 0.78 and 0.66, respectively (Bild and Wasson 1977). Watson has a flatter REE bulk pattern than MD, but is enriched compared to H chondrites, with $(La/Sm)_N$ and $(La/Yb)_N$ ratios of 1.20 and 1.18, respectively (Olsen et al. 1994).

Figure 5 shows the CI-normalized REE pattern for the phosphate phases of MD, compared to the REE patterns of these phases in equilibrated ordinary chondrites (EOC). From these patterns, it is clear that the bulk REE budget of MD is dominated by the REE content of the phosphate phases. The pattern of merrillite in MD shows the same trend as the EOC range, but is depleted compared to the EOC range, especially for the LREE. The REE pattern of apatite shows a similar trend and partly overlaps the EOC range, but is also depleted in LREE compared to the EOC range.

Oxygen Isotope Analysis

The oxygen isotope analysis performed on a MD silicate inclusion yields a mean $\Delta^{17}O$ of 0.71 ± 0.02‰, a $\delta^{18}O$ of 4.84 ± 0.45‰, and a $\delta^{17}O$ of 3.26 ± 0.26‰ (uncertainties reported as 2σ) (Figs. 6 and 7). According to Clayton et al. (1991), oxygen isotopic ranges for H chondrite falls are defined as in Figs. 6 and 7, where the oxygen isotopic composition of other IIE NMIM is also plotted. The $\Delta^{17}O$ value of MD resides completely in the range defined for the H chondrites ($\Delta^{17}O = 0.73 \pm 0.09$‰). MD does not reside, even within error, in the oxygen isotope range

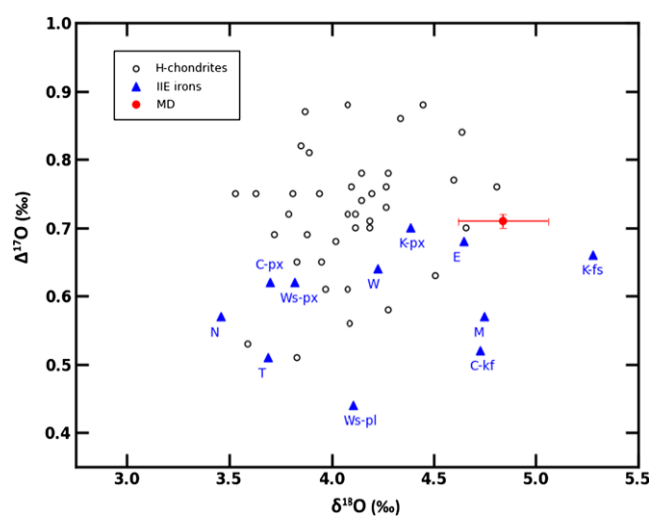

Fig. 7. Oxygen isotope compositions of the silicate inclusions of MD compared with silicate inclusions of other IIE irons (N = Netschaëvo, T = Techado, W = Watson, M = Miles, Ws-px = pyroxene in Weekeroo Station, Ws-pl = plagioclase in Weekeroo Station, C-px = pyroxene in Colomera, C-kf = K-feldspar in Colomera, K-px = pyroxene in Kodaikanal, K-fs = feldspar in Kodaikanal and E = Elga), and H chondrites. $\Delta^{17}O = \delta^{17}O - 0.52 * \delta^{18}O$. Data for IIE irons from Clayton and Mayeda (1996), and for H chondrites from Clayton et al. (1991).

of the other IIE NMIM, with an average $\Delta^{17}O$ of 0.59 ± 0.08‰ (1σ) (Clayton and Mayeda 1996). As this average value was calculated for the previously known IIE and MD constitutes a new member of this

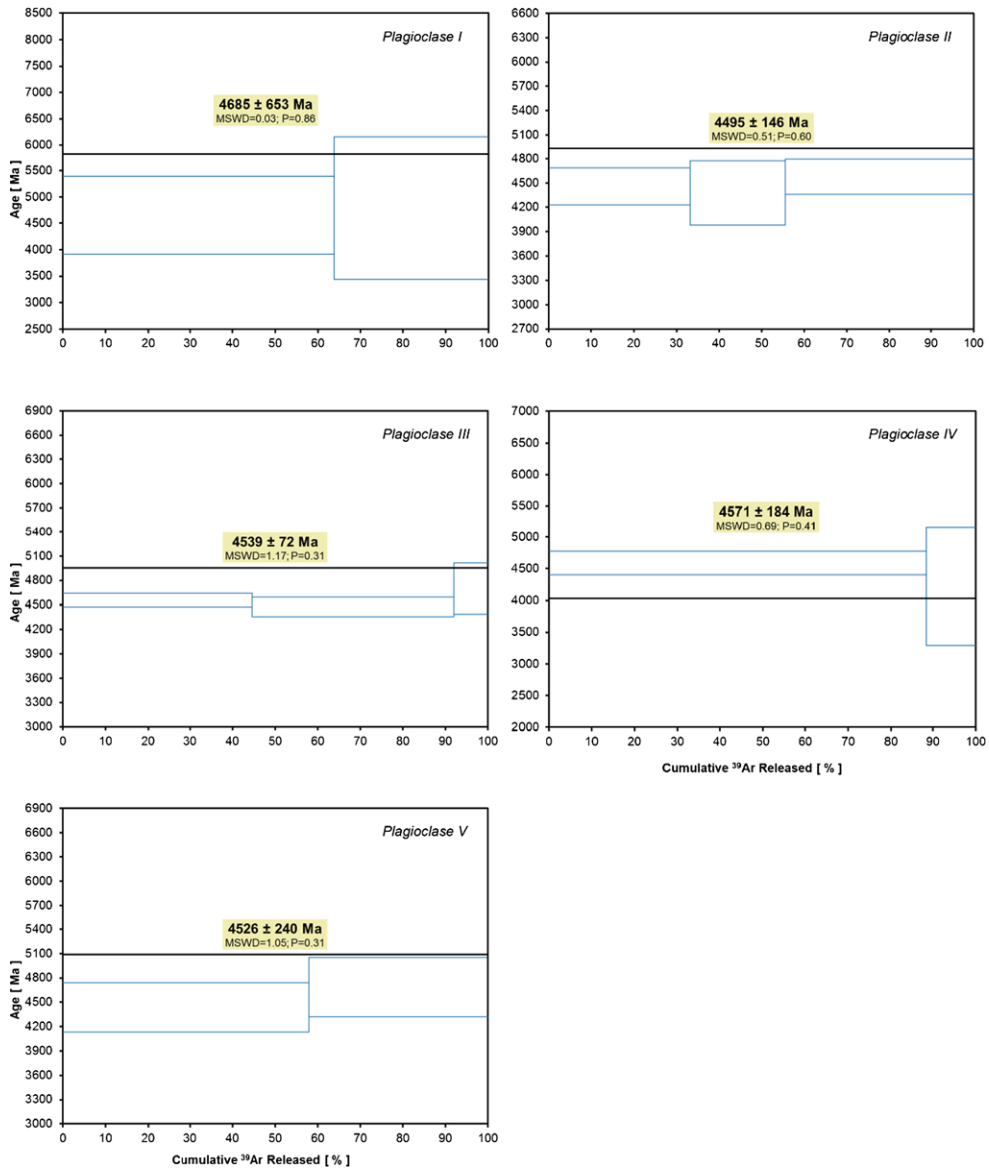

Fig. 8. $^{40}Ar/^{39}Ar$ age spectra measured for five coarse-grained plagioclase particles (<<150 μm in diameter each) of MD using laser step-heating. Ages have been calculated using the ^{40}K decay constants of Renne et al. (2011) and the R-value$_{(FC\ s/Hb3\ gr)}$ of Jourdan and Renne (2007). MSWD = Mean square weighted deviation; P = Probability; Bold line shows the segment of the age spectra included in the age calculation. This is 100% in all cases.

group based on siderophile element concentrations of its metal, its composition was not taken into account yet but can simply extend the IIE oxygen isotopic range. However, from Fig. 7, it is clear that the oxygen isotopes values measured in MD silicate inclusions suggest a straightforward affinity with the H chondrites.

$^{40}Ar/^{39}Ar$ Age

Five individual plagioclase grains were analyzed as individual crystals because of the possibility that they record different thermal histories (Vogel and Renne 2008). The five individual crystals yielded concordant ages including 100% of the gas but distributed over only two or three steps in each case, and with a rather poor precision. The five ages are 4685 ± 653 (P = 0.86), 4571 ± 184 (P = 0.41), 4539 ± 72 (P = 0.31), 4526 ± 240 (P = 0.31), and 4495 ± 146 (P = 0.60) Ma (Fig. 8). For this discussion, these ages are statistically indistinguishable and yield a weighted mean $^{40}Ar/^{39}Ar$ age of 4536 ± 59 Ma (P = 0.95; Fig. 9), which indicates an early formation/cooling age of the plagioclase.

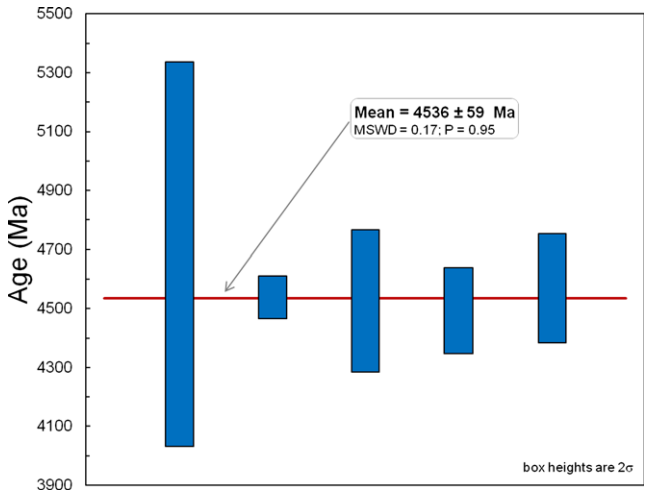

Fig. 9. A weighted mean age of 4536 ± 59 Ma (P = 0.95) has been calculated from the five individual plagioclase ages presented in Fig. 8. Full external error propagation using the optimization model of Renne et al. (2010) and R-value$_{(FCs/Hb3\ gr)}$ uncertainty of Jourdan and Renne (2007) yields an external uncertainty of ± [59] Ma.

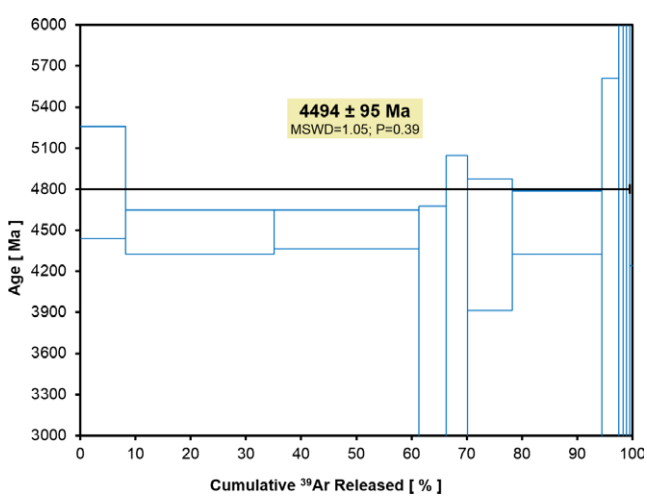

Fig. 10. $^{40}Ar/^{39}Ar$ age spectra measured for a pool of 10 fine-grained pyroxene particles (120–150 μm in diameter each) of MD using laser step-heating. A weighted mean age of 4494 ± 95 Ma (P = 0.39) has been calculated from these grains.

Because the pyroxene grains contain very little K_2O, these had to be analyzed in a pool of 10 grains despite the possibility of age mixture. However, Ar closure temperature (600–700 °C; Cassata et al. 2010) and activation energy for pyroxene are much higher than for plagioclase (250–300 °C; Cassata and Renne 2013). As such, pyroxene is insensitive to midtemperature perturbation, but rather loses its Ar over a very narrow range of temperature once the pyroxene closure temperature is reached. This spike diffusion

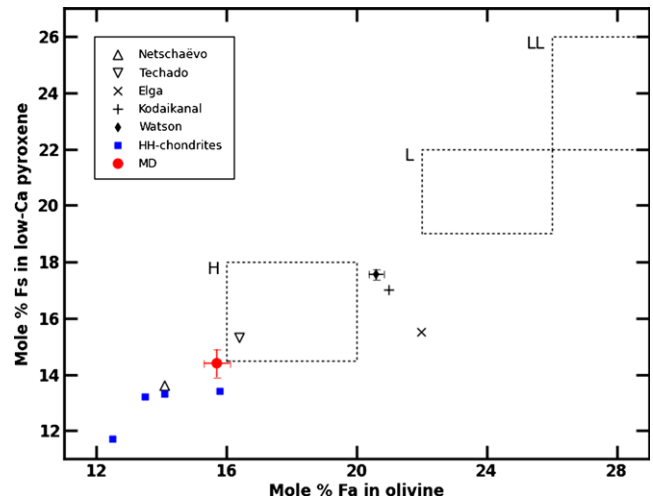

Fig. 11. Fs versus Fa molar contents of low-Ca pyroxenes and olivines for MD compared with other IIE irons, HH (Willaroy, Suwahib, Cerro los Calvos, and Burnwell), H, L, and LL chondrites. Data for IIE meteorites are from Olsen et al. (1994); for HH chondrites from Scott et al. (1985), Whitlock et al. (1991), and Russell et al. (1998); and for H, L, and LL chondrites from Brearley and Jones (1998).

characteristic of pyroxene is likely to constrain the thermochronological history of all the pyroxene grains to record either their crystallization ages or alternatively (and more realistically), to the impact that formed the MD silicates. The pyroxene yielded a well-developed $^{40}Ar/^{39}Ar$ plateau age of 4494 ± 95 Ma (P = 0.39; Fig. 10). The fact that the plateau age does not show any age mixing trend, suggests that indeed the pyroxene crystals recorded a unique age, at least within error.

Despite the relatively large error associated with those ages, both plagioclase and pyroxene $^{40}Ar/^{39}Ar$ ages are identical within analytical uncertainty and indicate that MD belongs to the "old group" (together with Techado, Colomera, Weekeroo Station, and Miles), with formation ages around 4.5 Ga (Bogard et al. 2000). Unfortunately, the errors associated with the $^{40}Ar/^{39}Ar$ ages for plagioclase and pyroxene are too large to allow an evaluation of the cooling rate based on the difference in the Ar closure temperature for both minerals.

DISCUSSION

Classification of MD

Based on the Ni, Ga, Ge, and Ir concentrations measured in the metal phase, this meteorite can be classified as IIE (see the Metal Host section). With a mass of 435 kg, the RBINS MD piece is the largest recovered IIE iron. Together with the Mont Dieu

fragments collected in 1994, representing a mass of 360 kg, the meteorite makes up a total mass of 795 kg.

Classification of Silicate Inclusions

The mineralogical assemblage present in the silicate inclusions of MD is clearly of chondritic nature, consisting of low-Ca pyroxene, olivine, plagioclase, metallic Fe-Ni, troilite, phosphates, and chromite. More importantly, relict chondrules are present. The bulk composition shows strong similarities with that of ordinary chondrites, more specifically the H chondrites (Table 4). The Fa and Fs molar contents of olivine and low-Ca pyroxene in MD overlap, within error, with the Fa and Fs ranges defined for H chondrites by Brearley and Jones (1998) (Fig. 11). The Fa and Fs molar content of MD does not overlap with the Fa range of 17.3–20.2 defined by Rubin (1990) nor with the Fs range of 15.7–18.1 defined by Gomes and Keil (1980) for H chondrites. Although the Fa and Fs molar contents of olivine and low-Ca pyroxene in MD demonstrate the same trend as observed for H chondrites, these do not strictly overlap with the H-group, as MD olivines and low-Ca pyroxenes are slightly more reduced (Fig. 11). This variation can be accounted for by a variety of scenarios, some of which are discussed below.

First of all, it is possible that the original silicate material of MD was a low FeO chondrite that plots along an extension of the H–L–LL trend (Fig. 11). Several such meteorites, also called HH chondrites, are reported in the literature (Bild and Wasson 1977; Wasson et al. 1993; Russell et al. 1998; Troiano et al. 2011). These chondrites have low Fa in olivine and/or Fs in pyroxene and lower $\Delta^{17}O$ values compared to H chondrites (Russell et al. 1998). According to Bild and Wasson (1977), Netschaëvo could also belong to the HH chondrites. This is also suggested by Rubin (1990), who argues that Netschaëvo could represent a member of a new OC group that is more reduced than H chondrites. Although several authors argue that these meteorites make up a new group of ordinary chondrites, Wasson et al. (1993) state that these meteorites were originally H or L chondrites that have been reduced during metamorphism. In the case of Netschaëvo, reduction could have occurred during the incorporation of the silicate phase into the metal host (Russell et al. 1998). Most of the HH chondrites are finds, meaning that terrestrial weathering and chemical disequilibrium can overprint their original composition. Despite these processes that possibly altered their parent material, true HH chondrites do exist. For example, the Burnwell meteorite, which is a fall and, therefore, has a composition not affected by weathering, has a lower Fa and Fs value, a higher Fe-Ni content, and a lower $\Delta^{17}O$ composition than H chondrites (Russell et al. 1998). However, given the scarcity of this type of chondrite, the observation that MD does not have a lower $\Delta^{17}O$ value (Fig. 7) and the fact that MD is a find, lend limited support to the hypothesis that the parent material of MD was an HH chondrite.

In a second scenario, Fa and Fs contents could have been affected by thermal processing, as higher Fa and Fs contents are observed in differentiated IIE silicates (Ruzicka 2014). Indeed, Fig. 11 clearly shows that the Fa and Fs values for differentiated IIE are less reduced compared to H chondrites. The relation between thermal processing and oxidation of silicates is also observed by Rubin (1990), who found that olivine Fa values tend to increase with increasing petrologic type. An increasing Fa and Fs trend is observed in the direction of Netschaëvo—Techado—Watson/Kodaikanal/Elga. Because MD holds several chondrules, possesses abundant Fe-Ni and troilite, and differs in mineralogy compared to the differentiated IIE, it is clear that thermal processing must have been very limited. If thermal processing had occurred, the Fa and Fs values would evolve into the more oxidized direction. For these reasons, this scenario can be ruled out.

A third possible explanation is reduction in FeO after the incorporation of the silicate material in the iron host. This possibility is also brought up by Russell et al. (1998) to explain the more reduced composition of Netschaëvo compared to H chondrites. In Weekeroo Station, reduction also occurred for minerals close to the Fe host (Ruzicka et al. 1999). Although Weekeroo Station is a differentiated IIE and tends toward more oxidized compositions for pyroxene, reduction occurred in the pyroxenes closest to the metal host, resulting in Fs values around 20 mole%, compared to 28–35 Fs mole% in other pyroxenes (Ruzicka et al. 1999). This process likely also occurred in MD, when silicates came in contact with the Fe host and the Fe melt within the silicates.

Taking all these arguments into account, the most plausible explanation for the reduced nature of MD silicate inclusions seems to be reduction after incorporation in the metal host. This would indicate that MD originated as an H chondrite.

Despite these similarities, important differences can also be observed. Compared to H-chondrites, the silicate inclusions of MD have a lower proportion of silicate minerals (70%), while silicate minerals make up about 86 vol% of H chondrites (Table 2). High-Ca pyroxene is not present in the silicate phase of MD. Compared to H chondrites, MD is highly enriched in troilite and phosphates (22% and 2% in MD versus

4.25% and 0.71% in H-chondrites), while the Fe-Ni proportion is lower (5% in MD versus 8.21% in H chondrites) (Table 2). The veins present in MD, containing angular silicate and troilite clasts, are also uncommon in H chondrites.

The silicate minerals in the inclusions show textural and geochemical similarities with type 5–6 chondrites: the silicates are generally coarse-grained, olivine, low-Ca pyroxene, and plagioclase; have homogeneous compositions; plagioclase is present as larger grains (up to 150 μm); no twinned pyroxene is observed; and chondrules are not abundant.

The oxygen isotope analysis also links the silicate inclusions of MD to the H chondrites, although the effect of terrestrial alteration, which can influence the oxygen isotopic composition, needs to be evaluated. MD shows evidence of terrestrial alteration: Fe-Ni and troilite present in this meteorite are to a certain extent replaced by Fe-oxides. In addition, the sampling zone of the inclusion studied here was close to the edge of the meteorite. Based on visual examination of the prepared polished sections, approximately 80% and 50% of Fe-Ni and troilite, respectively, is altered. This is clear from the compositions of these phases but also from their rusty appearance. Studies of meteorite samples from hot and cold deserts indicate that metal is the phase most susceptible to terrestrial alteration, followed by sulphides and silicates (Lee and Bland 2004; Al-Kathiri et al. 2005; Bland et al. 2006). Based on the scale of weathering in ordinary chondrites (Wlotzka 1993), a weathering grade of W3 can be assigned to the RBINS MD piece analyzed in this work. Metal and troilite are strongly altered, but not entirely, and there are no, or only incipient, signs of weathering of the silicate minerals.

When terrestrial alteration takes place, terrestrial water infiltrates the meteorite and the isotopic value shifts toward more terrestrial values, and thus closer to the terrestrial fractionation line (TFL) (Greenwood et al. 2012). Antarctic meteorites affected by terrestrial weathering show a shift in $\delta^{18}O$ value toward isotopically lighter values, whereas weathered non-Antarctic meteorites display a shift toward heavier $\delta^{18}O$ values (Greenwood and Franchi 2004). Unfortunately, studies quantifying the effect of terrestrial alteration on the oxygen isotopic composition of meteorites are sparse. A group of ordinary chondrites finds, both hot desert and Antarctic samples, was studied by Bland et al. (2000) in an attempt to quantify the degree of weathering. These authors concluded that alteration is a two-stage process. During the first phase, the shift in the isotopic value is negligible. Only during a second phase, at ~25% of the alteration, a shift toward more terrestrial values for both groups takes place. However, a recent study of achondrites by Greenwood et al. (2012) indicates that oxidation of metal and sulfide can shift the isotope value, even during the earliest stages of terrestrial alteration. These authors also observed that terrestrial alteration has an important effect on the variation in the $\delta^{18}O$ value, while the $\Delta^{17}O$ is less affected and reflects most likely the intrinsic primary oxygen isotope signature. Oxygen isotope values are also significantly enhanced if samples are acid leached prior to the analysis (Greenwood et al. 2008).

In the case of MD, which is a find, infiltration of terrestrial water could have influenced its isotope composition. However, prior to the analysis, silicate chips showing rust were removed and the selected material was washed with acetone. The result obtained for MD (Fig. 7) gives the highest $\Delta^{17}O$ value reported for all IIE. If terrestrial alteration has influenced its composition, this would have resulted in a shift toward the TFL (Bland et al. 2000). Because this is not observed, we conclude that the measured $\Delta^{17}O$ is a minimum value. The $\delta^{18}O$ value is situated toward the higher boundary of the IIE range (Fig. 6) and may reflect some degree of terrestrial weathering.

The bulk REE pattern of MD silicate (Fig. 4) does not correspond to the average H chondrites and is difficult to interpret. Based on the observed pattern, some fractionation seems to have occurred, although no petrographic evidence for this process is observed. Other IIE meteorites have REE patterns that can be explained by a combination of processes, including whole-rock melting, partial melting, and metamorphism (Ruzicka 2014). More detailed studies are necessary to find out if such processes have affected the REE pattern of MD and to what extent.

Alteration could also influence the $^{40}Ar/^{39}Ar$ age defined for MD. The $^{40}Ar/^{39}Ar$ chronometer, in particular for plagioclase, is very sensitive to alteration, especially if the alteration overprint is a recent event compared to the age being measured (Verati and Jourdan 2014). Despite its extreme sensitivity to alteration, none of the plagioclase crystals analyzed in this study shows any sign of age disturbance or partial age resetting in any of the steps measured (Figs. 8 and 9). Furthermore, none of the plagioclase analyzed shows any trace of contamination by atmospheric argon, which usually accompanies alteration or weathering of plagioclase (Baksi 2007). Such an atmospheric contamination is even easier to detect for extraterrestrial plagioclase that does not contain any atmospheric Ar in its pristine state. These observations suggest that the K/Ar system has not been perturbed by terrestrial alteration, and by extension that the effect of alteration on the isotopic system of the MD silicates should be minimal. We can conclude that the age defined for MD

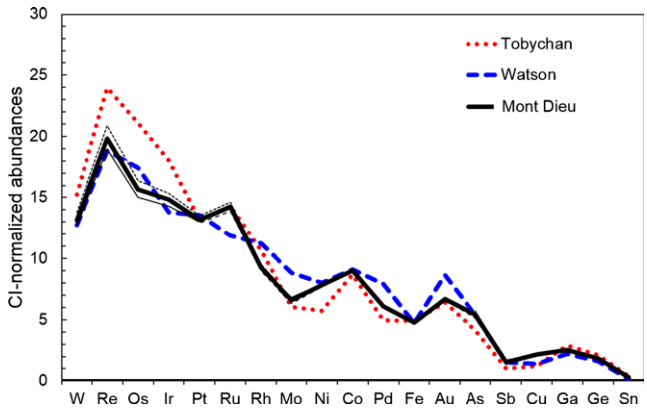

Fig. 12. CI-normalized (Anders and Grevesse 1989) metal composition of MD (average in black thick line, individual analyses in thin black lines), compared with Watson IIE and Tobychan IIE. Data for Watson and Tobychan from Teplyakova et al. (2012).

and the classification as a member of the old IIE group is reliable.

To summarize, based on the oxygen isotope composition, the bulk composition, the overall mineralogy, and the average Fa and Fs molar content, the silicate inclusions of MD can clearly be linked to the H chondrites.

Comparison With Other IIE Irons

As MD is a new member of the IIE group, it should be positioned within this group. In this section, MD is compared to other members of the IIE group. Features present in the metal and silicate inclusions of MD are compared with those observed in the most primitive members Netschaëvo, Techado, and Watson.

Metal Phase

Internally, there is very little fractionation within MD, but the compatible siderophile elements are systematically higher in metal from the polished mount, while these same elements are systematically lower in Area 2, a chunk of metal from MD, distinct from Areas 1 or 3. The average metal composition for MD is shown as the bold black line in Fig. 12. The siderophile element abundances of average MD metal are compared with those of two other IIE irons from Teplyakova et al. (2012), Tobychan, and Watson, and the patterns are very similar (Fig. 12). The degree of fractionation observed in the most compatible siderophiles (Re, Os, Ir) is nearly identical between Watson and MD. Abundances of Ga, Ge, and Sn are also very similar, but the abundance of Cu in MD is higher than in the other IIE. Based on the siderophile element pattern, MD metal appears to be an IIE iron.

Silicate Phase

The shape and distribution of the silicate inclusions in MD (Fig. 1b) best match those of the inclusions in Netschaëvo. However, Rubin et al. (2001) argued that the angular clasts in Netschaëvo once fit together, but are now separated by a few millimeters of metal veins, which is not the case for MD. The irregular inclusions in MD also resemble the irregular inclusion present in Techado (Casanova et al. 1995), although the degree of stretching of the silicate is much more pronounced in Techado.

In MD, as well as in Netschaëvo, relict chondrules occur (Bunch et al. 1970; Bild and Wasson 1977; Rubin 1990). Except for these two meteorites, chondrules have not been observed in the silicate phases of IIE where extensive melting and/or extensive recrystallization resulted in the loss of chondritic textures. In Netschaëvo, a barred olivine chondrule, a radial pyroxene chondrule, and several chondrules consisting of interlocking blebs of pyroxene and olivine are reported to occur (Bunch et al. 1970). These authors labeled these last types of chondrules as "unusual" because these do not correspond to a specific type of chondrule. These unusual chondrules are very similar to the recrystallized chondrules observed in MD.

The nature of olivine and low-Ca pyroxene in MD, with Fa and Fs molar contents of 15.7 ± 0.4 and 14.4 ± 0.5 mole%, respectively, is slightly more reduced compared to H chondrites (Fig. 11). This is also the case for Netschaëvo, although much more pronounced, with Fa and Fs molar contents of 14.1 and 13.6 mole%, respectively (Mittlefehldt et al. 1998) (Fig. 11). Rubin (1990) reports a similar composition with Fa and Fs molar contents of 14.3 ± 0.3 and 14.0 ± 0.2 mole%, respectively. The composition of the olivines and low-Ca pyroxenes of MD is intermediate between Netschaëvo and Techado ($Fa_{16.4}$, $Fs_{15.3}Wo_{1.6}$) (Mittlefehldt et al. 1998). The total iron and silicate content of MD exhibit a similar trend toward the composition of Netschaëvo (Table 4), with the iron content decreasing toward the differentiated IIE NMIM. Troilite is present as a major mineral phase in Netschaëvo (in the chondrules as well as matrix), Techado (Bunch et al. 1970; Casanova et al. 1995), and MD. In the other IIE containing silicate inclusions, troilite is present as an accessory phase, mainly along the margins of the inclusions.

The oxygen isotope signature of the silicates in MD clearly resides within the range observed for H chondrites, indicating a straightforward link to this group. This is not the case for Netschaëvo and Techado that exhibit lower $\Delta^{17}O$ values (0.57‰ and 0.51‰, respectively) than the H chondrites (Fig. 7) (Clayton

and Mayeda 1996). Netschaëvo has been forged after its recovery and locally reheated to temperatures above 1000 °C (Buchwald 1975), potentially altering its oxygen isotope composition. However, a study that performed high precision oxygen isotopic measurements on IIE confirms the previously defined oxygen isotopic composition of Netschaëvo ($\Delta^{17}O$ of 0.58‰; McDermott et al. 2011).

Except for silicate veinlets present in Elga (Osadchii et al. 1981), and millimeter-sized metal veins separating the silicate clasts in Netschaëvo (Rubin et al. 2001), no veins have been reported in IIE silicates. It seems that the thick Fe-P veins filled with clasts constitute a feature unique to MD.

The geochemical and textural features indicate that MD represents a primitive member of the IIE group. Although there are important differences between Netschaëvo and MD, including the age (~4.5 Gyr for MD and ~3.6 Gyr for Netschaëvo) and the oxygen isotopic composition, MD shares many features with Netschaëvo, as listed above. Therefore, we propose that these two meteorites together make up the most primitive subgroup in the IIE group. As a consequence, the IIE group is recommended to be sorted from primitive to differentiated as follows (1) MD and Netschaëvo; (2) Techado; (3) Watson; (4) Miles and Weekeroo Station; and (5) Kodaikanal, Colomera, and Elga.

Formation

In this section, a formation scenario is presented, taking into account all the observations and analyses presented and performed on MD. In the following paragraphs, several aspects of this process will be highlighted separately.

Thermal Processing of Silicate Inclusions

The silicate inclusions in MD were to a certain extent heated. Several textural features in the phosphate, troilite, and metal phases indicate that these minerals were once molten. Their irregular, elongated shapes that crosscut and enclose silicate minerals; the widespread occurrence of metal melt globules; the metal and troilite veinlets; the thick veins containing a groundmass consisting of a mixture of Fe, Ni, and P; together with the metal-troilite and metal-phosphate intergrowths are all evidence of such a thermal event. However, the melting seems to have been limited in extent. The silicate minerals in the inclusions do not show clear evidence of melting, no melt pockets are observed, and several clearly recognizable and well-delineated chondrules are still present. The relative higher abundance of phosphate in MD compared to H chondrites (2 vol% versus 0.7 vol%, respectively) and the absence of clinopyroxene in MD (in H chondrites clinopyroxene makes up 4.7 vol%), could be explained by a subsolidus reaction between P-bearing metal and clinopyroxene. Locally, phosphorus diffuses out of the metal and oxidizes to form a Ca-phosphate, with the Ca provided by clinopyroxene by diffusion. This type of phosphate-forming reaction has been proposed to occur in stony and iron meteorites (Olsen and Fuchs 1967; Murrell and Burnett 1983; Harlow et al. 1984), in the H6 metallic-melt chondrite breccia Portales Valley (Ruzicka et al. 2005), and also in the H6 chondrite impact-melt breccia Spade (Rubin and Jones 2003). This reaction can also explain the preferred concentration of large phosphate close to the metal–silicate interface. The occurrence of this process is supported by the composition of the phosphate minerals in MD, that corresponds well with that of average H chondrites (Van Schmus and Ribbe 1969; Curtis and Schmitt 1979), and by the REE patterns of the phosphates in MD (Fig. 5), that show trends similar to the EOC, meaning that chemical processing was limited. The fact that both phosphates in MD are depleted in LREE is consistent with subsolidus diffusion, because LREE diffuse more slowly than HREE from phosphate (Cherniak 2000). As suggested by Rubin and Jones (2003), the oxygen needed to form the phosphates could have been supplied by reduction in FeO to metallic Fe. This phenomenon likely also occurred in the inclusions of MD, and would be consistent with the hypothesis discussed in Classification of Silicate Inclusions section that states that the slightly more reduced nature of the silicates in MD compared to H chondrites was probably a consequence of FeO reduction to Fe metal.

Given the combination of melted troilite, metal, and phosphates and pristine silicates, the heating event must have been limited to around the Fe-FeS eutectic (~920 °C; Wasson et al. 1980a), to prevent melting of the silicates (the silicate solidus is ~1080 °C; Wasson et al. 1980b). The event must have been followed by relatively fast cooling, preventing the complete loss of the chondritic texture and textural transition of the barred olivine chondrules.

The heat source that formed these features was probably also responsible for the incorporation of silicate inclusions into metallic material. Most IIE formation models are based on impact and/or internal heating processes to explain this incorporation mechanism (Ruzicka 2014). The next paragraph will focus on the arguments against and in favor of these scenarios.

Impact Versus Internal Heating

Internal heating is a slow process with a homogeneous distribution of heat. In the case of MD,

there is no evidence of a homogeneous process, as some parts of the silicate phase are better preserved than others, as evidenced by the preservation of several chondrules, and the different morphologies of the silicate inclusions, sometimes showing angular features (e.g., in the thick veins). During the slow process of internal heating that can be spread over more than 1 million years (Rubin et al. 2001), the gravity-driven melt separation would exclude chondritic clasts as the result of the difference in density between metal and silicate (Tomkins et al. 2013a). As the influence of gravity is minimal in melt migration during impact events, metallic melt moving in response to pressure gradients can entrain chondritic clasts without being excluded due to buoyancy effects (Tomkins et al. 2013a, 2013b). In the case of MD, a rapid mixing and fast cooling process is needed to incorporate the silicate inclusions into a metallic body and, therefore, the scenario of an impact event is preferred. Because the pressure differentials produced during high-energy impact events are very high, the influence of the gravitational gradient becomes negligible and fluid flow is controlled by deformation-driven pressure gradients. As viscosities are lower in metal and sulfide melt compared to silicate, these will migrate quickly and as a consequence form large metal accumulations (Tomkins et al. 2013a). This means that the impact event also provides a mechanism to concentrate metal. An impact formation scenario could also be a viable process for the formation of other primitive IIE irons such as Netschaëvo and Techado, although additional investigations will be necessary to constrain specific conditions required for these meteorites.

As already pointed out by Rubin and Jones (2003), this process, and the accompanying heterogeneous distribution of heat, can also explain the fact that certain chondrules were obliterated, while other chondrules preserved well. The occurrence of silicate darkening (Rubin 1992), expressed as the widespread occurrence of small metal and troilite melt globules, supports this hypothesis, as this feature is caused by impact heating of metallic Fe-Ni and troilite grains (Rubin and Jones 2003). The presence of the thick metal veins containing angular silicate and troilite clasts is reminiscent of metal-dominated veins in and metal-cemented breccias of ordinary chondrites described by Rubin et al. (2001) and Ruzicka et al. (2005). These structures are interpreted to have formed through immiscible melt migration as a result of impact heating (Rubin et al. 2001; Ruzicka et al. 2005). A similar process is likely responsible for the production of the veins in MD. Partial melting experiments using chondrites have shown that veining structures can only be produced after heating the sample for 1 week at 700–1000 °C (McSween et al. 1978) or for 1 h at 1200 °C (Feldstein et al. 2001). The nature of the experimentally produced veins cannot be compared with the veins present in MD, as the experimentally produced veins are small (1–2 μm thick) and not interconnected. Rushmer et al. (2000) studied chondrites heated under conditions of differential stress. Coarse metal and troilite vein structures, called cataclastic structures, were produced that contain silicate clasts of different grain sizes. These features are very similar to the veins in MD and could indicate that impact played a role in their formation. Rushmer et al. (2000) also showed that preferential movement of metal and sulfide is possible throughout a solid silicate matrix, and thus without, or with very limited, melting of the silicate portion.

The fact that the silicate inclusion of MD examined here is classified as shock stage S1 based on the absence of shock features in the silicate minerals does not exclude the role of impact in the formation of MD since annealing during conditions near the melting point may erase shock features (Rubin 2004). Shock features can be very local and heterogeneously distributed as well. The presence of silicate darkening, thick metal veins, and the requirement of a heterogeneous heat source to explain all observations strongly suggest an impact origin.

Aside from the primitive IIE NMIM, the silicate inclusions in MD also show similarities with other meteorites, such as the H6 chondrite impact-melt breccia Spade (Rubin and Jones 2003) and the H6 metallic-melt chondrite breccia Portales Valley (Rubin et al. 2001; Ruzicka et al. 2005), which are also associated with impact events. Petrographic features present in MD silicates strongly resemble features present in these meteorites, such as relict chondrules, pincer-shaped plagioclase patches, fine-grained regions of silicates, the occurrence of numerous small blebs of Fe-Ni and troilite spread throughout mafic silicate grains, and troilite-metal and phosphate-metal intergrowths.

$^{40}Ar/^{39}Ar$ ages on large plagioclase grains were obtained on IAB iron meteorites by Vogel and Renne (2008), showing a significant range of apparent ages (4.3–4.5 Ga) suggesting that each of the individual silicate grains had a different thermal history and thus, came from different locations within the IAB parent body before the impact. In this study, we recovered only a few plagioclase and pyroxene crystals with grain size <<150 μm. As such, these crystals yielded $^{40}Ar/^{39}Ar$ ages with an average precision that is not sufficient to test any age variation among the grains and rather suggest that within errors, these ages are indistinguishable at 4536 ± 59 Ma. The pyroxene age of

4494 ± 95 Ma is also imprecise and therefore does not allow testing the impact hypothesis.

Widmanstätten Pattern

One of the major problems with the scenario of fast cooling after an impact event, necessary to preserve chondrules and chondritic textures, is the nature of the metal host. As mentioned above, MD is classified as a fine octahedrite, with bandwidths of ~0.3 mm. According to the kamacite bandwidth method of Short and Goldstein (1967), the width of the kamacite bands can directly be linked to the cooling rate of the iron meteorite, as kamacite bands grow at the expense of taenite during the cooling of an iron meteorite (Goldstein et al. 2009). Slower cooling rates correspond to a better developed WP and wider bandwidths. Nucleation of the WP is dependent on the original P and Ni content of the meteorite and on the path followed through the Fe-Ni-P diagram during cooling. In general, the WP develops in the 800–500 °C temperature range at a constant cooling rate (Goldstein et al. 2009).

The slow cooling necessary to develop the 0.3 mm wide kamacite bands conflicts with the fast cooling required to preserve the silicate phase. A situation where these two conditions are fulfilled simultaneously could be an impact-formed metal melt pool located at the near surface of an asteroid, where heat can dissipate more quickly. A fast cooling of the silicate can be expected near the edge of the melt pool in the temperature range of ~1080–800 °C. The peak temperature must have been between 1080 and 920 °C as this is the temperature needed to melt metal, troilite, and phosphate, but not silicates (Goldstein et al. 2009). After a first phase of relatively rapid cooling, the rest of the metal pool must have cooled more slowly, from 800 °C on, to develop the observed WP.

Timing and Nature of the Parent Body

Given the clear H chondritic nature of the silicate inclusions of MD, the impact event likely occurred on the H chondritic parent body. Although the petrologic type of the chondritic material before the impact took place is hard to evaluate, it was likely of high petrologic type because of the presence of very well-equilibrated silicate minerals (Table 3) and a low amount of relict chondrules. The modal abundance of chondrules in average H6 chondrites is 11.4 vol% (Rubin and Jones 2003). In MD, this is ~6 area%, indicating that about 50% of the chondrules in MD were obliterated. If the initial material was of low petrologic type (type 3), 65–75 vol% of chondrules were originally present in the chondrite (Rubin and Jones 2003) suggesting that at least 90% of chondrules in MD were destroyed. In the latter case, the degree of melting should have been extensive and clear evidence of silicate melting should be preserved in MD. As this is not the case, the reasoning presented here indicates that the target material should have been of high petrologic type. Another explanation is that because 85% of all chondrules in OC are porphyritic, they recrystallize easily and integrate with the coarsening of the matrix during metamorphism. In this case, the target material could have been of low petrologic type, provided that enough time was available for metamorphism. Because MD probably cooled relatively quickly, as argued previously, not enough time was available for this process. Given that the silicate minerals are well equilibrated in MD, this should have been the case already before the impact, indicating that the initial material of MD was probably of high petrologic type.

The impact event that led to the formation of MD took place very early on in the solar system, as indicated by the $^{40}Ar/^{39}Ar$ ages of ~4.5 Ga obtained for both on pyroxene and plagioclase. The consistency between the ages determined for plagioclase and pyroxene grains indicates that the silicate inclusions have not been thermally perturbed since the formation event. For example, subsequent heating events by impacts would have affected the K/Ar system in pyroxene and plagioclase differently (e.g., Kennedy et al. 2013; Jourdan et al. 2014), but the shape of all the age spectra suggest that both phases had the K/Ar system fully closed after 4.5 Ga. Because the determined ages encompass the age of the solar system within error, it could be related to the formation of the chondrite parent body or to the MD-forming impact event. The $^{40}Ar/^{39}Ar$ data constrain the latter event between the formation of the solar system and a minimum age of 4.48 Ga as given by the uncertainty range of the plagioclase age.

CONCLUSIONS

The 435 kg piece of the Mont Dieu meteorites characterized in this work indicates that Mont Dieu is a new primitive silicate-bearing member of the IIE irons. Silicate inclusions studied in this piece contain relict chondrules, about half of which are well-preserved barred olivine chondrules, while the other half are recrystallized. The mineral assemblage is of chondritic nature, containing olivine, low-Ca pyroxene, plagioclase, troilite, Fe-Ni, phosphates, and chromite. The major element composition also fits best to ordinary chondrites, more specifically H chondrites. The Fa and Fs molar content falls in the H range ($Fa_{15.7 \pm 0.4}$ and $Fs_{14.4 \pm 0.5}$) as does the oxygen isotopic composition ($\Delta^{17}O = 0.71 \pm 0.02‰$). The combination of

these observations supports the notion that MD originated as an H chondrite.

For the mixing of H chondrite and metallic material and the formation of IIE irons, an impact-based origin is favored. This hypothesis is based on the observation of a series of features, including silicate darkening, thick metal veins containing angular clasts, and the need for a heterogeneous heat source.

Based on $^{40}Ar/^{39}Ar$ analyses of pyroxene and plagioclase inclusions, MD belongs to the "old" ~4.5 Ga IIE group, together with Techado, Colomera, Weekeroo Station, and Miles. Within the mineralogical IIE sequence, MD can be assigned to the most primitive subgroup, together with Netschaëvo. MD and Netschaëvo are the only IIE irons that contain chondrules in their silicate inclusions. These meteorites also share similar major element compositions, but have different ages (MD belongs to the old ~4.5 Ga group while Netschaëvo is part of the ~3.6 Ga group) and oxygen isotopic compositions (MD is clearly of H chondritic signature while this is less straightforward for Netschäevo).

The silicate inclusions in MD also share characteristics with other meteorites, such as ordinary chondritic breccias Spade and Portales Valley, primitive achondrites, and primitive IAB silicate inclusions. Together with these meteorites, MD represents a stage in a continuous series between chondrites and differentiated bodies. Although its formation history could not fully be constrained here, MD provides a valuable contribution to a more complete understanding of planetary differentiation processes, because metal accumulations caused by such impact events can contribute to the core formation process, as already suggested by Tomkins et al. (2013a).

Acknowledgments—The authors thank the RBINS, Herman Goethals and Marleen De Ceukelaire, for providing the samples. We also thank Oscar Steenhaut, Peter Czaja, and Kitty Baert for their technical support on the SEM, EPMA, and Raman spectrometry, respectively. John Valley assisted in oxygen isotopes analysis and reviewed an earlier version of this paper. We thank Jan Hertogen for carrying out the ICP-OES analysis. Editorial handling by Nancy Chabot and reviews by Alan Rubin and Alex Ruzicka are gratefully acknowledged. Nadia Van Roosbroek and Vinciane Debaille thank the FRS-FNRS for funding through an incentive grant. Lidia Pittarello is supported by the Belgian Science Policy Office (BELSPO). Steven Goderis is a postdoctoral fellow of the Research Foundation-Flanders (FWO). Philippe Claeys thanks the Research Foundation Flanders (FWO; grants: G.A078.11 and G.0021.11). Munir Humayun was supported by the NASA Cosmochemistry program (grant# NNX13AI06G). This research has been partly funded by the Interuniversity Attraction Poles Programme "Planet Topers" initiated by BELSPO.

Editorial Handling—Dr. Nancy Chabot

REFERENCES

Al-Kathiri A., Hofmann B. A., Jull A. J. T., and Gnos P. 2005. Weathering of meteorites from Oman: Correlation of chemical/mineralogical weathering proxies with ^{14}C terrestrial ages and the influence of soil chemistry. *Meteoritics & Planetary Science* 40:1215–1239.

Anders E. and Grevesse N. 1989. Abundances of the elements: Meteoritic and solar system. *Geochimica et Cosmochimica Acta* 53:197–214.

Armstrong J. T., Kennedy A. K., Carpenter P. K., and Albee A. L. 1990. Petrography and trace element chemistry of Colomera (IIE) silicate inclusions: Rhyolitic plums in the pudding. Proceedings, 21st Lunar and Planetary Science Conference. pp. 22–23.

Baksi A. K. 2007. A quantitative tool for detecting alteration in undisturbed rocks and minerals—I: Water, chemical weathering, and atmospheric argon. *Geological Society of America Special Paper* 430:285–303.

Bence A. E. and Burnett D. S. 1969. Chemistry and mineralogy of the silicates and metal of the Kodaikanal meteorite. *Geochimica et Cosmochimica Acta* 33:387–407.

Bild R. W. and Wasson J. T. 1977. Netschaëvo: A new class of chondritic meteorite. *Science* 197:58–62.

Bland P. A., Lee M. R., Sexton A. S., Franchi I. A., Fallick A. E. T., Miller M. F., Cadogan J. M., Berry F. J., and Pillinger C. T. 2000. Aqueous alteration without a pronounced oxygen-isotopic shift: Implications for the asteroidal processing of chondritic materials. *Meteoritics & Planetary Science* 35:1387–1395.

Bland P. A., Zolensky M. E., Benedix G. K., and Sephton M. A. 2006. Weathering of chondritic meteorites. In *Meteorites and the early solar system*, edited by Lauretta D. and McSween H. Y. Jr. Tucson, Arizona: The University of Arizona Press. pp. 853–867.

Bogard D. D., Garrison D. H., and McCoy T. J. 2000. Chronology and petrology of silicates from IIE iron meteorites: Evidence of a complex parent body evolution. *Geochimica et Cosmochimica Acta* 64:2133–2154.

Brearley A. J. and Jones R. H. 1998. Chondritic meteorites. In *Planetary materials*, edited by Papike J. J. Albuquerque, New Mexico: Reviews in Mineralogy Press. pp. 3.1–3.191.

Buchwald V. F. 1975. *Handbook of iron meteorites*. Berkeley, California: University of California Press. p. 1418.

Bunch T. E., Keil K., and Olsen E. 1970. Mineralogy and petrology of silicate inclusions in iron meteorites. *Contributions to Mineralogy and Petrology* 25:297–340.

Burnett D. S. and Wasserburg G. J. 1967. Evidence for the formation of an iron meteorite at 3.8 x 10^9 years. *Earth and Planetary Science Letters* 2:137–147.

Campbell A. J., Humayun M., and Weisberg M. K. 2002. Siderophile element constraints on the formation of metal in the metal-rich chondrites Bencubbin, Weatherford, and Gujba. *Geochimica et Cosmochimica Acta* 66:647–660.

Casanova I., Graf T., and Marti K. 1995. Discovery of an unmelted H-chondrite inclusion in an iron meteorite. *Science* 268:540–542.

Cassata W. S. and Renne P. R. 2013. Systematic variations of argon diffusion in feldspars and implications for thermochronometry. *Geochimica et Cosmochimica Acta* 112:251–287.

Cassata W. S., Shuster D. L., Renne P. R., and Weiss B. P. 2010. Evidence for shock heating and constraints on Martian surface temperatures revealed by $^{40}Ar/^{39}Ar$ thermochronometry of Martian meteorites. *Geochimica et Cosmochimica Acta* 74:6900–6920.

Cherniak D. J. 2000. Rare earth element diffusion in apatite. *Geochimica et Cosmochimica Acta* 64:3871–3885.

Choi B.-G., Ouyang X., and Wasson J. T. 1995. Classification and origin of IAB and IIICD iron meteorites. *Geochimica et Cosmochimica Acta* 59:593–612.

Clayton R. and Mayeda T. 1996. Oxygen isotope studies of achondrites. *Geochimica et Cosmochimica Acta* 60:1999–2017.

Clayton R., Mayeda T., Goswami J. N., and Olsen E. 1991. Oxygen isotope studies of ordinary chondrites. *Geochimica et Cosmochimica Acta* 55:2317–2337.

Cosca M., Stunitz H., Bourgeix A. L., and Lee J. P. 2011. $^{40}Ar^*$ loss in experimentally deformed muscovite and biotite with implications for $^{40}Ar/^{39}Ar$ geochronology of naturally deformed rocks. *Geochimica et Cosmochimica Acta* 75:7759–7778.

Crozaz G., Pellas P., Bourot-Denise M., de Chazal S. M., Fiéne C., Lundberg L. L., and Zinner E. 1989. Plutonium, uranium and rare earths in the phosphates of ordinary chondrites—The quest for a chronometer. *Earth and Planetary Science Letters* 93:157–169.

Curtis D. B. and Schmitt R. A. 1979. The petrogenesis of L-6 chondrites: Insights from the chemistry of minerals. *Geochimica et Cosmochimica Acta* 43:1091–1103.

Desrousseaux A., Doukhan J. C., Fieni C., Perron C., Jeannot J. P., Lavielle B., Renaud D., Van Duysen J. C., Caffee M., and Nishiizumi K. 1996. A new iron meteorite from France. *Meteoritics & Planetary Science* 31:A36–A37.

Feldstein S. N., Jones R. H., and Papike J. J. 2001. Disequilibrium partial melting experiments on the Leedey L6 chondrite: Textural controls on melting processes. *Meteoritics & Planetary Science* 36:1421–1441.

Gaffey M. J. and Gilbert S. L. 1998. Asteroid 6 Hebe: The probable parent body of the H-type ordinary chondrites and the IIE iron meteorites. *Meteoritics & Planetary Science* 33:1281–1295.

Goldstein J. I., Scott E. R. D., and Chabot N. L. 2009. Iron meteorites: Crystallization, thermal history, parent bodies, and origin. *Chemie der Erde* 69:293–325.

Gomes C. B. and Keil K. 1980. *Brazilian stone meteorites*. Albuquerque, New Mexico: University of New Mexico Press. 161 p.

Greenwood R. C. and Franchi I. A. 2004. Alteration and metamorphism of CO3 chondrites: Evidence from oxygen and carbon isotopes. *Meteoritics & Planetary Science* 39:1823–1838.

Greenwood R. C., Gibson J. M., and Franchi I. A. 2008. Hot and cold weathering determining the oxygen isotope composition of achondrites. *Meteoritics & Planetary Science* 43:A182.

Greenwood R. C., Franchi I. A., Gibson J. M., and Benedix G. K. 2012. Oxygen isotope variation in primitive achondrites: The influence of primordial, asteroidal and terrestrial processes. *Geochimica et Cosmochimica Acta* 94:146–163.

Grossman J. N. 1997. The Meteoritical Bulletin No. 81. *Meteoritics & Planetary Science* 32:A159–A166.

Harlow G. E., Delaney J. S., Nehru C. E., and Prinz M. 1984. Metamorphic reactions in mesosiderites: Origin of abundant phosphate and silica. *Geochimica et Cosmochimica Acta* 46:339–348.

Heilbronner R. 2000. Automatic grain boundary detection and grain size analysis using polarization micrographs or orientation images. *Journal of Structural Geology* 22:969–981.

Hsu W. 2003. Rare earth element geochemistry and petrogenesis of Miles (IIE) silicate inclusions. *Geochimica et Cosmochimica Acta* 67:4807–4821.

Humayun M. 2012. Chondrule cooling rates inferred from diffusive profiles in metal lumps from the Acfer 097 CR2 chondrite. *Meteoritics & Planetary Science* 47:1191–1208.

Humayun M., Simon S. B., and Grossman L. 2007. Tungsten and hafnium distribution in calcium-aluminium inclusions (CAIs) from Allende and Efremovka. *Geochimica et Cosmochimica Acta* 71:4609–4627.

Ikeda Y. and Prinz M. 1996. Petrology of silicate inclusions in the Miles IIE iron. *Proceedings of the NIPR Symposim on Antarctic Meteorites* 9:143–173.

Ikeda Y., Ebihara M., and Prinz M. 1997. Petrology and chemistry of the Miles IIE iron. I: Description and petrology of twenty new silicate inclusions. *Antarctic Meteorite Research* 10:355–372.

Jochum K. P. and Stoll B. 2008. Reference materials for elemental and isotopic analyses by LA-(MC)-ICP-MS: Successes and outstanding needs. *Laser Ablation ICP-MS in the Earth Sciences: Current Practices and Outstanding Issues*. *Mineralogical Association of Canada* 40:147–168.

Jourdan F. and Renne P. R. 2007. Age calibration of the Fish Canyon sanidine $^{40}Ar/^{39}Ar$ dating standard using primary K-Ar standards. *Geochimica et Cosmochimica Acta* 71:387–402.

Jourdan F., Verati C., and Féraud G. 2006. Intercalibration of the Hb3gr $^{40}Ar/^{39}Ar$ dating standard. *Chemical Geology* 231:177–189.

Jourdan F., Benedix G., Eroglu E., Bland P., and Bouvier A. 2014. $^{40}Ar/^{39}Ar$ impact ages and time-temperature argon diffusion history of the Bunburra Rockhole anomalous basaltic achondrite. *Geochimica et Cosmochimica Acta* 140:391–409.

Kennedy T., Jourdan F., Bevan A. W. R., Gee M. A. M., and Frew A. 2013. Impact history of the HED parent body (ies) clarified by new $^{40}Ar/^{40}Ar$ analyses of four HED meteorites and one anomalous basaltic achondrite. *Geochimica et Cosmochimica Acta* 115:162–182.

Koppers A. A. P. 2002. ArArCALC-software for $^{40}Ar/^{39}Ar$ age calculations. *Computers & Geosciences* 28:605–619.

Kurat G., Zinner E., and Varela M. E. 2007. Trace elements studies of silicate-rich inclusions in the Guin (UNGR) and Kodaikanal (IIE) iron meteorites. *Meteoritics & Planetary Science* 42:1441–1463.

Lee J.-Y., Marti K., Severinghaus J. P., Kawamura K., Yoo H.-S., Lee J. B., and Kim J. S. 2006. A redetermination of the isotopic abundance of atmospheric Ar. *Geochimica et Cosmochimica Acta* 70:4507–4512.

Lee M. R. and Bland P. A. 2004. Mechanisms of weathering of meteorites recovered from hot and cold deserts and the

formation of phyllosilicates. *Geochimica et Cosmochimica Acta* 68:893–916.

Martin C., Debaille V., Lanari P., Goderis S., Vandendael I., Vanhaecke F., Vidal O., and Claeys P. 2013. REE and Hf distribution among mineral phases in the CV–CK clan: A way to explain present-day Hf isotopic variations in chondrites. *Geochimica et Cosmochimica Acta* 120: 496–513.

McCoy T. J. 1995. Silicate-bearing IIE irons: Early mixing and differentiation in a core-mantle environment and shock resetting of ages. *Meteoritics* 30:542–543.

McDermott K., Greenwood R. C., Franchi I. A., Anand M., and Scott E. R. D. 2011. Oxygen isotopic and petrological constraints on the origin and relationship of IIE iron meteorites and H chondrites (abstract #2673). 42nd Lunar and Planetary Science Conference. CD-ROM.

McDonough W. F. and Sun S. S. 1995. The composition of the Earth. *Chemical Geology* 120:223–253.

McSween H. Y. Jr., Taylor L. A., and Lipschutz M. E. 1978. Metamorphic effects in experimentally heated Krymka (L3) chondrite. Proceedings, 9th Lunar and Planetary Science Conference. pp. 1437–1447.

Mittlefehldt D. W., McCoy T. J., Goodrich C. A., and Kracher A. 1998. Non-chondritic meteorites from asteroidal bodies. In *Planetary materials*, edited by Papike J. J. Albuquerque, New Mexico: Reviews in Mineralogy Press. pp. 4.1–4.195.

Murrell M. T. and Burnett D. S. 1983. The behavior of actinides, phosphorus, and rare earth elements during chondrite metamorphism. *Geochimica et Cosmochimica Acta* 47:1999–2014.

Olsen E. and Fuchs L. H. 1967. The state of oxidation of some iron meteorites. *Icarus* 6:242–253.

Olsen E., and Jarosewich E. 1971. Chondrules: First occurence in an iron meteorite. *Science* 174:583–585.

Olsen E., Davis A., Clarke R. S. J., Schultz L., Weber H. W., Clayton R., Mayeda T., Jarosewich E., Sylvester P., Grossman L., Wang M.-S., Lipschutz M. E., Steele I. M., and Schwade J. 1994. Watson: A new link in the IIE iron chain. *Meteoritics* 29:200–213.

Osadchii E. G., Baryshnikova G. V., and Novikov G. V. 1981. The Elga meteorite: Silicate inclusions and shock metamorphism. Proceedings, 12th Lunar and Planetary Science Conference. pp. 1049–1068.

Prinz M., Nehru C. E., and Delaney J. S. 1982. Sombrerete: An iron with highly fractionated amphibole-bearing Na-P silicate inclusions. Proceedings, 13th Lunar and Planetary Science Conference. pp. 634–635.

Renne P. R., Mundil R., Balco G., Min K., and Ludwig K. R. 2010. Joint determination of ^{40}K decay constants and ^{40}Ar*/^{40}K for the Fish Canyon sanidine standard, and improved accuracy for ^{40}Ar/^{39}Ar geochronology. *Geochimica et Cosmochimica Acta* 74:5349–5367.

Renne P. R., Balco G., Ludwig K. R., Mundil R., and Min K. 2011. Response to the comment by Schwarz W.H., Kossert K., Trieloff M., and Hopp J. 2011 on "Joint determination of ^{40}K decay constants and ^{40}Ar*/^{40}K for the Fish Canyon sanidine standard, and improved accuracy for ^{40}Ar/^{39}Ar geochronology" by Renne P.R., Mundil R., Balco G., Min K. and Ludwig K.R. 2010. *Geochimica et Cosmochimica Acta* 75:5097–5100.

Rubin A. E. 1990. Kamacite and olivine in ordinary chondrites: Intergroup and intragroup relationships. *Geochimica et Cosmochimica Acta* 54:1217–1232.

Rubin A. E. 1992. A shock-metamorphic model for silicate darkening and compositionally variable plagioclase in CK and ordinary chondrites. *Geochimica et Cosmochimica Acta* 56:1705–1714.

Rubin A. E. 2004. Postshock annealing and post annealing shock in equilibrated ordinary chondrites: Implications for the thermal and shock histories of chondritic asteroids. *Geochimica et Cosmochimica Acta* 68:673–689.

Rubin A. E. and Jones R. H. 2003. Spade: An H chondrite impact-melt breccia that experienced post-shock annealing. *Meteoritics & Planetary Science* 38:1507–1520.

Rubin A. E., Jerde E. A., Zong P., Wasson J. T., Westcott J. W., Mayeda T. K., and Clayton R. N. 1986. Properties of the Guin ungrouped iron meteorite: The origin of Guin and of group-IIE irons. *Earth and Planetary Science Letters* 76:209–226.

Rubin A. E., Moller F. U., Wasson J. T., and Carlson W. D. 2001. The Portales Valley meteorite breccia: Evidence for impact-induced melting and metamorphism of an ordinary chondrite. *Geochimica et Cosmochimica Acta* 65:323–342.

Rubin A. E., Huber H., and Wasson J. T. 2009. Possible impact-induced refractory-lithophile fractionations in EL chondrites. *Geochimica et Cosmochimica Acta* 73:1523–1537.

Rushmer T., Gaetani G., and Jones J. H. 2000. Chondrites under stress: What can they tell us about core formation processes? (abstract #1673). 31st Lunar and Planetary Science Conference. CD-ROM.

Russell S. S., McCoy T. J., Jarosewich E., and Ash R. D. 1998. The Burnwell, Kentucky, low iron oxide chondrite fall: Description, classification and origin. *Meteoritics & Planetary Science* 33:853–856.

Ruzicka A. M. 2014. Silicate-bearing iron meteorites and their implications for the evolution of asteroidal parent bodies. *Chemie der Erde—Geochemistry* 74:3–48.

Ruzicka A. M. and Hutson M. 2010. Comparitive petrology of silicates in the Udei Station (IAB) and Miles (IIE) iron meteorites: Implications for the origin of silicate-bearing irons. *Geochimica et Cosmochimica Acta* 74:394–433.

Ruzicka A. M., Fowler G. W., Snyder G. A., Prinz M., Papike J. J., and Taylor L. A. 1999. Petrogenesis of silicate inclusions in the Weekeroo Station IIE iron meteorite: Differentiation, remelting, and dynamic mixing. *Geochimica et Cosmochimica Acta* 63:2123–2143.

Ruzicka A. M., Killgore M., Mittlefehldt D. W., and Fries M. D. 2005. Portales Valley: Petrology of a metallic-melt meteorite breccia. *Meteoritics & Planetary Science* 40:261–295.

Scott E. R. D. 1972. Chemical fractionation in iron meteorites and its interpretation. *Geochimica et Cosmochimica Acta* 36:1205–1236.

Scott E. R. D. and Wasson J. T. 1976. Chemical classification of iron meteorites—VIII. Groups IC. IIE. IIIF and 97 other irons. *Geochimica et Cosmochimica Acta* 40:103–115.

Scott E. R. D., Clayton R. N., and Mayeda T. K. 1985. Properties and genesis of two anomalous Type 3 chondrites, Suwahib (buwah) and Willaroy (abstract). 16th Lunar and Planetary Science Conference. p. 749.

Short J. J. and Goldstein J. I. 1967. Rapid methods of determining cooling rates of iron and stony iron meteorites. *Science* 156:59–61.

Spicuzza M. J., Day J. M. D., Taylor L. A., and Valley J. W. 2007. Oxygen isotope constraints on the origin and

differentiation of the Moon. *Earth and Planetary Science Letters* 253:254–265.

Stöffler D., Keil K., and Scott E. R. D. 1991. Shock metamorphism of ordinary chondrites. *Geochimica et Cosmochimica Acta* 55:3845–3867.

Takeda H., Hsu W., and Huss G. R. 2003. Mineralogy of silicate inclusions of the Colomera IIE iron and crystallization of Cr-diopside and alkali feldspar from a partial melt. *Geochimica et Cosmochimica Acta* 67:2269–2288.

Teplyakova S. N., Humayun M., Lorenz C. A., and Ivanova M. A. 2012. A common parent for IIE iron meteorites and H chondrites (abstract #1130). 43rd Lunar and Planetary Science Conference. CD-ROM.

Tomkins A. G., Weinberg R. F., Schaefer B. F., and Langendam A. 2013a. Disequilibrium melting and melt migration driven by impacts: Implications for rapid planetesimal core formation. *Geochimica et Cosmochimica Acta* 100:41–59.

Tomkins A. G., Mare E. R., and Raveggi M. 2013b. Fe-carbide and Fe-sulfide liquid immiscibility in IAB meteorite, Campo del Cielo: Implications for iron meteorite chemistry and planetesimal core compositions. *Geochimica et Cosmochimica Acta* 117:80–98.

Troiano J., Rumble D. III, Rivers M. L., and Friederich J. M. 2011. Compositions of three low-FeO ordinary chondrites: Indications of a common origin with the H chondrites. *Geochimica et Cosmochimica Acta* 75:6511–6519.

Underwood E. E. 1970. *Quantitative stereology*. Reading, Massachusetts: Boston: Addison-Wesley Publishing Company. 274 p.

Valley J. W., Kitchen N., Kohn M. J., Niendorf C. R., and Spicuzza M. J. 1995. UWG-2, a garnet standard for oxygen isotope ratios: Strategies for high precision and accuracy with laser heating. *Geochimica et Cosmochimica Acta* 59:5223–5231.

Van Schmus W. R. and Ribbe P. H. 1969. Composition of phosphate minerals in ordinary chondrites. *Geochimica et Cosmochimica Acta* 33:637–640.

Verati C. and Jourdan F. 2014. Modelling effect of sericitization of plagioclase on the $^{40}K/^{40}Ar$ and $^{40}Ar/^{39}Ar$ chronometers: Implication for dating basaltic rocks and mineral deposits. *Advances in $^{40}Ar/^{39}Ar$ Dating: From Archaeology to Planetary Sciences Special Publications 378:155–174*.

Vogel N., and Renne P. R. 2008. ^{40}Ar–^{39}Ar dating of plagioclase grain size separates from silicate inclusions in IAB iron meteorites and implications for the thermochronological evolution of the IAB parent body. *Geochimica et Cosmochimica Acta* 72:1231–1255.

Walker R. J., McDonough W. F., Honesto J., Chabot N., McCoy T. J., Ash R. D., and Bellucci J. J. 2008. Modeling fractional crystallization of group IVB iron meteorites. *Geochimica et Cosmochimica Acta* 72:2198–2216.

Wasserburg G. J., Sanz G. J., and Bence A. E. 1968. Potassium-feldspar phenocrysts in the surface of Colomera, an iron meteorite. *Science* 161:684–687.

Wasson J. T. 1985. *Meteorites—Their record of early solar system history*. New York: W.H. Freeman and Co. 267 p.

Wasson J. T. and Kallemeyn G. W. 1988. Compositions of chondrites. *Philosophical Transactions of the Royal Society of London. Series A, Mathematical and Physical Sciences* A325:535–544.

Wasson J. T. and Kallemeyn G. W. 2002. The IAB iron-meteorite complex: A group, five subgroups, numerous grouplets, closely related, mainly formed by crystal segregation in rapidly cooling melts. *Geochimica et Cosmochimica Acta* 66:2445–2473.

Wasson J. T. and Wang J. 1986. A nonmagmatic origin of group-IIE iron meteorites. *Geochimica et Cosmochimica Acta* 50:725–732.

Wasson J. T., Willis J., Wai C. M., and Kracher A. 1980a. Origin of iron meteorite groups IAB and IIICD. Proceedings, 11th Lunar and Planetary Science Conference. pp. 25–26.

Wasson J. T., Willis J., Wai C. M., and Kracher A. 1980b. Origin of iron meteorite groups IAB and IIICD. *Zeitschrift für Naturforschung* 35a:781–795.

Wasson J. T., Ouyang X., Wang J., and Jerde E. 1989. Chemical classification of iron meteorites: XI. Multi-element studies of 38 new irons and the high abundance of ungrouped irons from Antarctica. *Geochimica et Cosmochimica Acta* 53:735–744.

Wasson J. T., Rubin A. E., and Kallemeyn G. W. 1993. Reduction during metamorphism of four ordinary chondrites. *Geochimica et Cosmochimica Acta* 57:1867–1878.

Weisberg M. K., McCoy J. T., and Krot A. N. 2006. Systematics and evaluation of meteorite classification. In *Meteorites and the early solar system II*, edited by Lauretta D. and McSween H. Y. Jr. Tucson, Arizona: The University of Arizona Press. pp. 19–52.

Whitlock R., Lewis C. F., Clark J. C., and Moore C. B. 1991. The Cerro Los Calvos and La Banderia chondrites. *Meteoritics* 26:169–170.

Wlotzka F. 1993. A weathering scale for the ordinary chondrites. *Meteoritics* 28:460.

SUPPORTING INFORMATION

Additional supporting information may be found in the online version of this article:

Annex S1: Argon isotopic data corrected for blank, mass discrimination and radioactive decay